Computation of non-similar solution for magnetic pseudoplastic nanofluid flow over a circular cylinder with variable thermophysical properties and radiative flux

Received 25 April 2020
Revised 12 July 2020
Accepted 28 July 2020

Thameem Basha Hayath, Sivaraj Ramachandran and Ramachandra Prasad Vallampati
Department of Mathematics, School of Advanced Sciences, Vellore Institute of Technology, Vellore, India, and

O. Anwar Bég
Multi-Physical Engineering Sciences Group (MPESG), Department of Aeronautical/Mechanical Engineering, School of Science, Engineering and Environment (SEE), University of Salford, Salford, UK

Abstract

Purpose – Generally, in computational thermofluid dynamics, the thermophysical properties of fluids (e.g. viscosity and thermal conductivity) are considered as constant. However, in many applications, the variability of these properties plays a significant role in modifying transport characteristics while the temperature difference in the boundary layer is notable. These include drag reduction in heavy oil transport systems, petroleum purification and coating manufacturing. The purpose of this study is to develop, a comprehensive mathematical model, motivated by the last of these applications, to explore the impact of variable viscosity and variable thermal conductivity characteristics in magnetohydrodynamic non-Newtonian nanofluid enrobing boundary layer flow over a horizontal circular cylinder in the presence of cross-diffusion (Soret and Dufour effects) and appreciable thermal radiative heat transfer under a static radial magnetic field.

Design/methodology/approach – The Williamson pseudoplastic model is deployed for rheology of the nanofluid. Buongiorno's two-component model is used for nanoscale effects. The dimensionless nonlinear partial differential equations have been solved by using an implicit finite difference Keller box scheme. Extensive validation with earlier studies in the absence of nanoscale and variable property effects is included.

Findings – The influence of notable parameters such as Weissenberg number, variable viscosity, variable thermal conductivity, Soret and Dufour numbers on heat, mass and momentum characteristics are scrutinized and visualized via graphs and tables.

Research limitations/implications – Buongiorno (two-phase) nanofluid model is used to express the momentum, energy and concentration equations with the following assumptions. The laminar, steady, incompressible, free convective flow of Williamson nanofluid is considered. The body force is implemented in the momentum equation. The induced magnetic field strength is smaller than the external magnetic field and hence it is neglected. The Soret and Dufour effects are taken into consideration.

Practical implications – The variable viscosity and thermal conductivity are considered to investigate the fluid characteristic of Williamson nanofluid because of viscosity and thermal conductivity have a prime role in many industries such as petroleum refinement, food and beverages, petrochemical, coating manufacturing, power and environment.

International Journal of Numerical Methods for Heat & Fluid Flow
Vol. 31 No. 5, 2021
pp. 1475-1519

0961-5539
DOI 10.1108/HFF-04-2020-0236

Social implications – This fluid model displays exact rheological characteristics of bio-fluids and industrial fluids, for instance, blood, polymer melts/solutions, nail polish, paint, ketchup and whipped cream.

Originality/value – The outcomes disclose that the Williamson nanofluid velocity declines by enhancing the Lorentz hydromagnetic force in the radial direction. Thermal and nanoparticle concentration boundary layer thickness is enhanced with greater streamwise coordinate values. An increase in Dufour number or a decrease in Soret number slightly enhances the nanofluid temperature and thickens the thermal boundary layer. Flow deceleration is induced with greater viscosity parameter. Nanofluid temperature is elevated with greater Weissenberg number and thermophoresis nanoscale parameter.

Keywords Variable thermal conductivity, Variable viscosity, Magnetohydrodynamics, Buongiorno nanofluid model, Williamson rheological model

Paper type Research paper

Nomenclature

a = radius of the cylinder [m];
B_0 = strength of the constant magnetic field [$kgs^{-2}A^{-1}$];
C = concentration of the fluid [kgm^{-3}];
C_f^* = skin friction coefficient;
$(C_p)_f$ = specific heat of fluid [$Jkg^{-1}K^{-1}$];
$(C_p)_p$ = specific heat of particle [$Jkg^{-1}K^{-1}$];
C_S = concentration susceptibility [kgm^{-3}];
C_W = concentration at the surface [kgm^{-3}];
C_∞ = ambient concentration [kgm^{-3}];
D_B = Brownian diffusion [m^2s^{-1}];
D_u = Dufour number;
D_T = thermophoretic diffusion [m^2s^{-1}];
g_a = acceleration because of gravity [ms^{-2}];
Gr = Grashof number;
k_{0f} = constant fluid thermal conductivity [$Wm^{-1}K^{-1}$];
k_e = mean absorption coefficient [m^{-1}];
k_f = fluid thermal conductivity [$Wm^{-1}K^{-1}$];
K_T = thermal diffusion ratio [m^2s^{-1}];
M_a = magnetohydrodynamic parameter;
N_B = Brownian motion parameter;
N_r = species to thermal buoyancy ratio parameter;
N_T = thermophoresis parameters;
Nu^* = Nusselt number;
Pr = Prandtl number;
R_a = Rosseland conduction-radiation parameter;
Sc = Schmidt number;
Sh^* = Sherwood number;
S_r = Soret number;
T = temperature of the fluid [K];
T_m = mean fluid temperature [K];
T_W = temperature at the surface [K];
T_∞ = ambient temperature[K];

u, v = velocity components in x,y directions [ms^{-1}];
We = Weissenberg number; and
x, y = Cartesian coordinates [m].

Greek symbols
β_1 = coefficient of nonlinear thermal expansion [K^{-1}];
Γ = material constant;
γ^* = variable viscosity parameter;
δ^* = variable thermal conductivity parameter;
μ_f = dynamic viscosity [$kgm^{-1}s^{-1}$];
μ_{0f} = constant dynamic viscosity [$kgm^{-1}s^{-1}$];
ρ_{0f} = constant density of fluid [kgm^{-3}];
ρ_{0p} = constant density of particle [kgm^{-3}];
ν_{0f} = constant kinematic viscosity [m^2s^{-1}];
σ = electrical conductivity of fluid [Sm^{-1}];
σ_B = Stefan Boltzmann constant [$=1.3807 \times 10^{-23} JK^{-1}$];
τ = ratio between particle and base fluid
τ^* = shear stress sensor; and
Φ = azimuthal coordinate.

1. Introduction

Molecular transport in a binary mixture driven by a temperature gradient is known as the thermo-diffusion (Soret) effect, whereas energy flux caused by a concentration gradient is known as the diffusion-thermo (Dufour) effect. Collectively, these cross-diffusion effects are often neglected because the order of magnitude is smaller than effects expressed by means of Fourier and Fick laws. The Soret effect is quite important when higher density differences exist in fluid transport. Dufour effect is ineffective in the mixture of various liquids, but this effect has a highly notable impact in gasses. Soret and Dufour effects play a major role in a mixture of gases between very light (Hydrogen, Helium) and medium (Nitrogen, air) molecular weights as deployed in isotope separation. Heat transfer properties are strongly coupled with mass transfer properties when double-diffusive (thermo-solutal) convection is considered with the influence of Soret and Dufour numbers. Soret and Dufour effects are accounted in various engineering technologies and industrial processes including the solidification of binary alloys, crystal growth, contaminant transport in groundwater, pollutant movement, chemical reactors, magmatic geophysical flows, oceanography, underground treatment of nuclear waste materials and drying technologies (Beg *et al.*, 2009a, 2009b; Kumar and Sivaraj, 2013; Rashad and Chamkha, 2014; Raju and Sandeep, 2016; Reddy and Chamkha, 2016; Ruhaila *et al.*, 2017; Muthtamilselvan *et al.*, 2018). Sivaraj *et al.* (2019) examined the cross-diffusion (Soret and Dufour) effects on Casson fluid flow with variable fluid properties and observed that higher values of Dufour effect or lower values of the Soret effect elevate Casson fluid temperature. Makinde and Olanrewaju (2011a) discussed the time-dependent mixed convective flow over a moving permeable plate with the influence of Soret and Dufour effects and found that the velocity of the fluid decreases with an increase in the Soret effect. Pal *et al.* (2016) used a numerical method to explore the Soret and Dufour impacts on three different water-based nanofluids over a plate and deduced that the water nanofluid concentration decays as a result of increasing Dufour number with decreasing Soret number. Other studies include Beg *et al.* (2011) on micropolar

coating flows, Beg *et al.* (2019a) worked on magnetohydrodynamics ocean generators and very recently Bhatti *et al.* (2020) on ferro-magnetic transport properties.

The vast majority of analytical boundary layer flow studies have been confined to constant thermo-physical properties of the fluid. When there is a high-temperature difference between the surface and fluid in boundary layer, the thermo-physical properties of fluid can vary notably. Compared with other thermo-physical properties, the fluid viscosity is highly sensitive with temperature variations. For instance, in lubricating liquids, heat is produced as a result of internal friction which causes a change in the viscosity of the fluid. The absolute viscosity of water declines by 240% because of an increase in temperature from 100°C to 500°C. As a result, it is logical to consider variable viscosity to more precisely determine transport characteristics. Varying viscosity with respect to temperature arises in many branches of modern technology including smart coating enrobing, drawing of plastic films, surfacial spray deposition, glass fiber production, petroleum refinement, fabrication of thin film concentrating solar receivers, food processing, gas turbine film cooling and fluid film tribology (Makinde and Chinyoka, 2012; Kumar and Sivaraj, 2013; Manjunatha and Gireesha, 2016; Sheikholeslami and Rokni, 2017; Astanina *et al.*, 2019; Salahuddin *et al.*, 2019). Animasaun (2015) reported a numerical study of free convective flow of Casson fluid over a plate with the cross-diffusion and noticed that higher viscosity parameter values reduce the Casson fluid temperature. Hayat *et al.* (2016) analytically investigated the mixed convective time-dependent flow over an exponential surface in the presence of temperature-dependent viscosity. Reddy *et al.* (2018) used a Crank Nicholson scheme to analyze fluid transport properties and entropy generation of time-dependent viscoelastic polymeric fluid flow with variable viscosity and observed that varying viscosity parameter enhances total entropy generation. Mehmood *et al.* (2019) exhibited the influence of variable viscosity on non-orthogonal stagnation flow of Cu–water nanofluid for nano-polymeric solar gel coatings application and found that increasing nanoparticle volume fraction decelerates the fluid flow.

Non-Newtonian fluids are fluids which have viscosity shear-dependence in addition to shear-thinning/shear-thickening characteristics. These fluids have numerous industrial applications, including petroleum production, bionic hydrogels in robotics, chemical process industries, plastic polymers, ferrofluid lubricants, packaging materials for food preservation, cosmetic products and manufacture of optical fibers. Non-Newtonian fluids have complex rheological characteristics, so the flow properties of such fluids cannot be elucidated by a single rheological model. As a result, a diverse range of constitutive models including the Maxwell upper convected fluid, Williamson fluid, Johnson–Segalman fluid, Cross fluid, FENE-P fluid, Walter's B-fluid, PPT fluid, Casson fluid, Eringen micropolar fluid and Carreau fluid models have been proposed by various researchers. Transport characteristics of various non-Newtonian fluid models were investigated by several researchers (Makinde *et al.*, 2011b; Gaffar *et al.*, 2015; Latiff *et al.*, 2016; Durairaj *et al.*, 2017; Khan *et al.*, 2019; Nadeem *et al.*, 2017; Norouzi *et al.*, 2018; Bisht and Sharma, 2019; Basha *et al.*, 2020b). The Williamson fluid model is a popular industrial rheological model which is developed originally for analyzing molten plastic molding (Williamson, 1929). This fluid model expresses the exact behavior of pseudoplastic fluids which differ from ideal plastics in which there is no real yield value. Because of its shear-thinning nature, the Williamson fluid model is used to analyze many other industrial fluids and biofluids including blood, polymeric suspension, magnetic polymers, etc.

Nanofluids are very popular in recent years because of their superior thermal conductivity property (Das *et al.*, 2007). Recently, many researchers have theoretically and experimentally explored the heat transfer characteristics of various nanoparticles for several industrial processes, manufacturing processes and renewable energy applications (Mansoury *et al.*, 2019; Ma *et al.*, 2019; Basha *et al.*, 2019). Nanofluids have been examined with certain volume fractions to exhibit shear-thinning behavior and other rheological characteristics. Several

careful experimental studies have confirmed the strong non-Newtonian properties of nanofluids in a diverse array of applications ranging from thermal engineering systems (Anoop *et al.*, 2009; Chang *et al.*, 2019) to petroleum drilling fluids (Beg *et al.*, 2018). Laboratory testing of nanofluid thermal enhancement features with rheological behavior has been accompanied with several numerical investigations Hussanan *et al.* (2017) and Kang *et al.* (2014). Acharya *et al.* (2019) addressed the multi-slip impact on Williamson nanofluid flow from a sheet and noticed that the rate of heat transfer declines with an increment in velocity and thermal slips. Basha *et al.* (2020a) numerically explored the variable fluid property effects on Williamson nanofluid flow over three different geometries with wall slip mechanisms. Subbarayudu *et al.* (2020) used the Williamson nanofluid model to simulate blood flow over a wedge surface with radiation heat transfer and indicated that higher values of Weissenberg number (ratio of elastic to viscous forces) accentuate blood temperature.

An inspection of the literature has revealed that most of the computational studies on external boundary layer flows of nanofluids have analyzed the rheological characteristics by converting the basic governing equations with boundary conditions into ordinary differential equations with suitable initial conditions. Furthermore, many studies have ignored the variation of thermophysical properties and cross diffusion effects. The objective of the current work is therefore to present a more generalized two-dimensional approach to axisymmetric nanofluid boundary layer flow from a cylindrical body with thermal radiation. The Williamson–Buongiorno nanofluid model is considered with the influence of magnetohydrodynamics, Soret and Dufour effects. Rosseland's diffusion flux approximation is used for accounting the radiative heat transfer. These constitute the novelties of the present work. The Williamson nanofluid viscosity and thermal conductivity are considered as variable because of temperature difference. The steady-state conservation equations are transformed, rendered non-dimensional and then solved with appropriate wall and free stream conditions by means of unconditionally stable implicit finite difference Keller box scheme. Extensive contour plots are drawn to manifest the significance of diverse multi-physical parameters on the fluid transport characteristics. Verification of the accuracy of the Keller box method with earlier published works is presented. The simulations are relevant to high-temperature magnetic nano-polymer coating flow systems (Sheparovych *et al.*, 2006; Hong *et al.*, 2007; Sansom *et al.*, 2013; Dhumal *et al.*, 2015; Vshivkov and Rusinova, 2017; Beg *et al.*, 2019a).

2. Mathematical formulation

Figure 1 exhibits the schematic view of geometry for the present problem in a two-dimensional Cartesian coordinate system (x, y). The viscosity and thermal conductivity variation in natural convective, laminar, time independent, incompressible flow of electrically conducting Williamson nanofluid (magnetic nano-polymer) over a circular cylinder is considered. A magnetic field of uniform strength B_0 is applied radially. a is the radius of the cylinder and the coordinates x and y are taken along the circumference of the cylinder and normal to the cylinder, respectively. Changes in density for the buoyancy terms are determined by using the Boussinesq approximation. The constant temperature (T_W) and concentration (C_W) of the surface are presumed to be greater than the ambient temperature (T_∞) and ambient concentration (C_∞), respectively. The Buongiorno (two phase) nanofluid model (Buongiorno, 2006) is used to formulate the momentum, energy and nano-particle concentration equations with the following assumptions:

- The flow equation is accounting the body force.
- The induced magnetic field strength is smaller compared to the external magnetic field, and hence it is neglected (small magnetic Reynolds number).

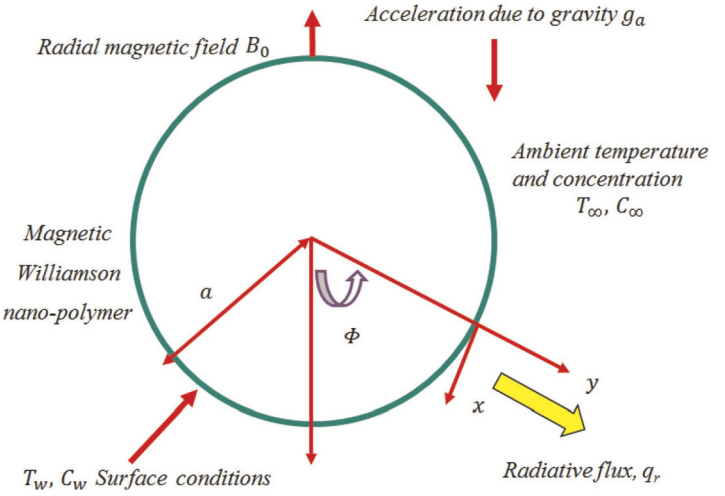

Figure 1.
Physical configuration of the problem

- Hall current, ion slip and Maxwell displacement currents are neglected.
- The circular cylinder is isothermal, iso-solutal and electrically insulated.
- Soret and Dufour effects are taken into consideration.

Based on the aforesaid considerations, the transport equations for the present problem in Cartesian coordinates (x, y) (Beg *et al.*, 2009b; Animasaun, 2015; Sivaraj *et al.*, 2019; Acharya *et al.*, 2019) can be shown to take the following form:

$$\frac{\partial u}{\partial x}+\frac{\partial v}{\partial y}=0, \tag{1}$$

$$u\frac{\partial u}{\partial x}+v\frac{\partial u}{\partial y}=\frac{1}{\rho_{0f}}\frac{\partial}{\partial y}\left[\mu_f(T)\frac{\partial u}{\partial y}\right]+\frac{\Gamma\sqrt{2}}{\rho_{0f}}\left[\frac{\partial}{\partial y}\left\{\left[\mu_f(T)\frac{\partial u}{\partial y}\right]\frac{\partial u}{\partial y}\right\}\right]-\frac{\sigma B_0^2}{\rho_{0f}}u + \frac{g_a}{\rho_{0f}}\left[(1-C_\infty)\rho_{0f}\beta_1(T-T_\infty)-(\rho_{0p}-\rho_{0f})(C-C_\infty)\right]\sin\left(\frac{x}{a}\right), \tag{2}$$

$$u\frac{\partial T}{\partial x}+v\frac{\partial T}{\partial y}=\frac{1}{\rho_{0f}(C_p)_f}\frac{\partial}{\partial y}\left[k_f(T)\frac{\partial T}{\partial y}\right]+\tau\left[D_B\frac{\partial C}{\partial y}\frac{\partial T}{\partial y}+\frac{D_T}{T_\infty}\left(\frac{\partial T}{\partial y}\right)^2\right] -\frac{1}{\rho_{0f}(C_p)_f}\frac{\partial q_r}{\partial y}+D_B\frac{K_T}{(C_p)_f C_S}\frac{\partial^2 C}{\partial y^2}, \tag{3}$$

$$u\frac{\partial C}{\partial x}+v\frac{\partial C}{\partial y}=D_B\frac{\partial^2 C}{\partial y^2}+\frac{D_T}{T_\infty}\frac{\partial^2 T}{\partial y^2}+D_B\frac{K_T}{T_m}\frac{\partial^2 T}{\partial y^2}. \tag{4}$$

It is to be noted that in the present formulation, the modified shear term in equation (2) is based on the extra stress tensor for a Williamson fluid (Williamson, 1929) which is defined

as $\chi = [\mu_{\infty f} + (\mu_{0f} + \mu_{\infty f})(1 - \tau^{*}\Lambda)^{-1}]A_1$, in which, consider $\mu_{\infty f} = 0$ and $\tau^{*}\Lambda < 1$ where the shear stress sensor is given by $\tau^{*} = \sqrt{\frac{\text{trac}(A_1^2)}{2}}$, $A_1 = \text{grad}\mathbf{V} + [\text{grad}\mathbf{V}]^{T}$.

The boundary conditions imposed are as follows:

$$\left.\begin{aligned} u = 0,\ v = 0,\ T = T_W,\ C = C_W \quad \text{at } y = 0, \\ u \to 0,\ T \to T_\infty,\ C \to C_\infty \quad \text{as } y \to \infty. \end{aligned}\right\} \tag{5}$$

where $\nu_{0f} = \frac{\mu_{0f}}{\rho_{0f}}$ and $\tau = \frac{\rho_{0p}(C_p)_p}{\rho_{0f}(C_p)_f}$.

The change in viscosity because of temperature is expressed as follows (Kumar and Sivaraj (2013)):

$$\frac{\mu_f(T)}{\mu_{0f}} = 1 - \gamma(T - T_\infty), \tag{6}$$

According to Sivaraj *et al.* (2019), the thermal conductivity variation is considered as a linear function in temperature.

$$\frac{k_f(T)}{k_{0f}} = 1 + \delta(T - T_\infty), \tag{7}$$

The unidirectional radiative heat flux (q_r) is written as follows (Basha *et al.*, 2019):

$$q_r = -\frac{4}{3}\frac{\sigma_B}{k_e}\left(\frac{\partial T^4}{\partial y}\right) = -\frac{16}{3}\frac{\sigma_B T_\infty^3}{k_e}\left(\frac{\partial T}{\partial y}\right), \tag{8}$$

The dimensional stream function ψ is defined according to the famous Cauchy–Riemann equations as $u = \frac{\partial(\psi(\xi,\eta))}{\partial x}$ and $v = -\frac{\partial(\psi(\xi,\eta))}{\partial y}$. In addition, the suitable non-similarity variables are considered as follows:

$$\left.\begin{aligned} \xi = \frac{x}{a},\ \eta = (Gr)^{\frac{1}{4}}\left(\frac{y}{a}\right),\ \psi = \xi f(Gr)^{\frac{1}{4}}\nu_{0f}, \\ T = T_\infty + \theta(T_W - T_\infty),\ C = C_\infty + \phi(C_W - C_\infty). \end{aligned}\right\} \tag{9}$$

By implementing the above variables, equations (2)–(4) are transformed to the following non-similar form in (ξ, η) coordinate system:

$$\begin{aligned} &(1 - \gamma^{*}\theta)f''' + 2We\xi(1 - \gamma^{*}\theta)f'''f'' - We\xi\gamma^{*}(f'')^2\theta' - \gamma^{*}f''\theta' \\ &\quad - (f')^2 + ff'' + \frac{\sin\xi}{\xi}(\theta - N_r\phi) - M_a f' = \xi\left[f'\frac{\partial f'}{\partial\xi} - f''\frac{\partial f}{\partial\xi}\right], \end{aligned} \tag{10}$$

$$\begin{aligned} &\frac{1}{\Pr}\left[(1 + \delta^{*}\theta) + \frac{4}{3R_a}\right]\theta'' + \frac{\delta^{*}(\theta')^2}{\Pr} + f\theta' + N_B\theta'\phi' \\ &\quad + N_T(\theta')^2 + D_u\phi'' = \xi\left[f'\frac{\partial\theta}{\partial\xi} - \theta'\frac{\partial f}{\partial\xi}\right], \end{aligned} \tag{11}$$

$$\frac{1}{Sc}\left[\phi'' + \frac{N_T}{N_B}\theta''\right] + f\phi' + S_r\,\theta'' = \xi\left[f'\frac{\partial\phi}{\partial\xi} - \phi'\frac{\partial f}{\partial\xi}\right]. \tag{12}$$

The transformed boundary conditions emerge as following:

$$\left.\begin{aligned} &f = f' = 0, \quad \theta = \phi = 1 \qquad \text{at } \eta = 0, \\ &f' \to 0, \qquad \theta \to 0, \quad \phi \to 0 \quad \text{as } \eta \to \infty. \end{aligned}\right\} \tag{13}$$

where $Gr = \frac{a^3(1-C_\infty)g_a\beta_1(T_W-T_\infty)}{\nu_{0f}^2}$, $We = \frac{\Gamma\nu_{0f}\sqrt{2}(Gr)^{3/4}}{a^2}$, $\Pr = \frac{\mu_{0f}(C_p)_f}{k_{0f}}$, $M_a = \frac{\sigma a^2 B_0^2}{(Gr)^{1/2}\nu_{0f}\rho_{0f}}$, $N_r = \frac{(\rho_{0p}-\rho_{0f})(C_W-C_\infty)}{(1-C_\infty)\rho_{0f}\beta_1(T_W-T_\infty)}$, $\gamma^* = \gamma(T_W - T_\infty)$, $N_B = \frac{\tau D_B(C_W-C_\infty)}{\nu_{0f}}$, $R_a = \frac{k_e k_{0f}}{4\sigma_B T_\infty^3}$, $N_T = \frac{\tau D_T(T_W-T_\infty)}{\nu_{0f}T_\infty}$, $\delta^* = \delta(T_W - T_\infty)$, $D_u = \frac{D_B K_T(C_W-C_\infty)}{\nu_{0f}C_S(C_p)_f(T_W-T_\infty)}$, $S_r = \frac{D_B K_T(T_W-T_\infty)}{\nu_{0f}T_m(C_W-C_\infty)}$, $Sc = \frac{\nu_{0f}}{D_B}$.

At the wall, dimensional forms of skin friction factor (C_f), heat transfer rate (N_u) and mass transfer rate (Sh) are expressed as follows:

$$\left.\begin{aligned} C_f &= \mu_f(T)\left[\frac{\partial u}{\partial y} + \frac{\Gamma}{2}\left(\frac{\partial u}{\partial y}\right)^2\right]_{y=0}, \\ Nu &= \frac{-a\left(k_f(T)\left[\frac{\partial T}{\partial y}\right]_{y=0} + (q_r)_{y=0}\right)}{k_{0f}(T_w - T_\infty)}, \\ Sh &= \frac{-a\left[\frac{\partial C}{\partial y}\right]_{y=0}}{(C_w - C_\infty)}. \end{aligned}\right\} \tag{14}$$

Using equations (6)–(9) in equation (14), the non-dimensional skin friction $\left(C_f^*\right)$, heat transfer rate (N_u^*) and mass transfer rate (Sh^*) are written as follows:

$$\left.\begin{aligned} C_f^* &= (1 - \gamma^*\theta)f''(0)\,\xi\left(1 + \xi\frac{We}{\sqrt{2}}f''(0)\right), \\ Nu^* &= -\left((1 + \delta^*\theta) + \frac{4}{3R_a}\right)\theta'(0), \\ Sh^* &= -\phi'(0). \end{aligned}\right\} \tag{15}$$

where $C_f^* = \frac{C_f a^2(Gr^{-3/4})}{\mu_{0f}\nu_{0f}}$, $Nu^* = Nu(\mathrm{Gr}^{-1/4})$, $Sh^* = Sh\,(\mathrm{Gr}^{-1/4})$.

3. Numerical method

Keller (1971) introduced a novel finite difference method called as Keller box method. This method is initially applied to solve parabolic problems. Later, this scheme is applied to solve various problems in laminar and turbulent boundary layer flows. The notable merits of this scheme are as follows:

- This scheme is well-organized, simple and flexible to program.
- In this scheme, there is no need to formulate any conditions to compute very close to the point of boundary layer separation.
- The variations in streamwise coordinate (ξ-direction) are rapidly admitted.
- The scheme has second-order accuracy and unconditionally stable.
- The non-similar solutions are obtained for boundary layer problems.

The similarity solution merely depends on the free stream velocity for the boundary layer equations. But the boundary layers may arise from various factors like the variation in wall temperature, free-stream velocity, suction/injection of fluid at the wall, and buoyancy effect. The non-similar solution can account these effects in the boundary layer. In addition, there is no clarity for ignoring certain streamwise derivatives in the similarity solution when converting the governing equations into dimensionless form. This dilutes the accuracy of the solutions. In a non-similar solution, only the auxiliary equations are removed from the fluid transport equations. Thus, the original fluid transport equations with boundary conditions remain same. Hence, it is expected that the non-similar solutions can provide more accurate results than the local-similarity solution.

The procedure to obtain the solution by using the Keller box method is given as follows:

- The *nth* order dimensionless equations are transformed into n first-order dimensionless equations.
- The transformed n first-order equations are discretized by using central differences approach.
- The algebraic equations are linearized by means of Newton's method.

The results are obtained by solving the block matrix system (block tri-diagonal elimination technique).

Step 1:

A new set of variables $u(\xi,\eta)$, $v(\xi,\eta)$,$s(\xi,\eta)$,$t(\xi,\eta)$,$g(\xi,\eta)$ and $p(\xi,\eta)$ are introduced to transform the *nth* order dimensionless equations into n first-order dimensionless equations, which depends on ξ and η.

The new set of variables are assumed as follows:

$$f = f, f' = u,\ u' = v,\ \theta = s,\ s' = t,\ \phi = g,\ g' = p, \tag{16}$$

By implementing the above variables, equations (10)–(12) are transformed to:

$$\begin{aligned}(1-\gamma^* s)v' + 2We\,\xi(1-\gamma^* s)v'v - We\,\xi\,\gamma^* v^2 t - \gamma^* v t \\ -u^2 + fv + B(s - N_r g) - M_a u = \xi\left[u\frac{\partial u}{\partial \xi} - v\frac{\partial f}{\partial \xi}\right]\end{aligned} \tag{17}$$

$$\begin{aligned}\frac{1}{\Pr}\left[(1+\delta^* s) + \frac{4}{3R_a}\right]t' + \frac{t^2\delta^*}{\Pr} + ft + N_B tp \\ + N_T t^2 + D_u p' = \xi\left[u\frac{\partial s}{\partial \xi} - t\frac{\partial f}{\partial \xi}\right]\end{aligned} \tag{18}$$

$$\frac{1}{Sc}\left[p' + \frac{N_T}{N_B}t'\right] + fp + S_r t' = \xi\left[u\frac{\partial g}{\partial \xi} - p\frac{\partial f}{\partial \xi}\right] \tag{19}$$

with the boundary conditions

$$\eta = 0: \quad u = 0, \quad f = 0, \quad s = 1, \quad g = 1 \tag{20}$$

$$\eta \to \infty: \quad u \to 0, \quad s \to 0, \quad g \to 0$$

Step 2:

The net point on the (ξ, η) plane is expressed using the following relations:

$$\xi^0 = 0, \quad \xi^i = \xi^{i-1} + k_i, \; i = 1, 2, 3 \ldots I, \tag{21}$$

$$\eta_0 = 0, \quad \eta_j = \eta_{j-1} + h_j, \; j = 1, 2, 3 \ldots J. \tag{22}$$

where k_i is $\Delta\xi$ spacing at the *ith* node, and h_j is $\Delta\eta$ spacing at *jth* node. The following discretizations are applied:

$$\left(\frac{\partial()}{\partial\xi}\right)_{j-\frac{1}{2}}^{i-\frac{1}{2}} = \frac{()_{j-\frac{1}{2}}^{i} - ()_{j-\frac{1}{2}}^{i-1}}{k_i}, \quad \left(\frac{\partial()}{\partial\eta}\right)_{j-\frac{1}{2}}^{i-\frac{1}{2}} = \frac{()_{j}^{i-\frac{1}{2}} - ()_{j-1}^{i-\frac{1}{2}}}{h_j}$$

$$()_{j}^{i-\frac{1}{2}} = \frac{()_{j}^{i-1} - ()_{j}^{i}}{2}, \quad ()_{j-\frac{1}{2}}^{i} = \frac{()_{j-1}^{i} - ()_{j}^{i}}{2}$$

At the midpoint $\left(\xi^i, \eta_{j-\frac{1}{2}}\right)$ between the segments (ξ^i, η_{j-1}) (ξ^i, η_j), the following central difference approximations are deployed:

$$f' = u \Rightarrow u_{j-\frac{1}{2}}^{i} = \frac{u_j^i + u_{j-1}^i}{2} = \frac{\left(f_j^i - f_{j-1}^i\right)}{h_j}, \tag{23}$$

$$u' = v \Rightarrow v_{j-\frac{1}{2}}^{i} = \frac{v_j^i + v_{j-1}^i}{2} = \frac{\left(u_j^i - u_{j-1}^i\right)}{h_j}, \tag{24}$$

$$s' = t \Rightarrow t_{j-\frac{1}{2}}^{i} = \frac{t_j^i + t_{j-1}^i}{2} = \frac{\left(s_j^i - s_{j-1}^i\right)}{h_j}, \tag{25}$$

$$g' = p \Rightarrow p_{j-\frac{1}{2}}^{i} = \frac{p_j^i + p_{j-1}^i}{2} = \frac{\left(g_j^i - g_{j-1}^i\right)}{h_j}, \tag{26}$$

First-order PDE equations (16)–(19) are approximated by centering at $\left(\xi^{i-\frac{1}{2}}, \eta_{j-\frac{1}{2}}\right)$ from the rectangle points (P_1,P_2,P_3 and P_4) and the following equations are obtained:

$$\left.\begin{aligned}
&\left(\frac{v_j^i - v_{j-1}^i}{h_j}\right) - \gamma^* s_{j-1/2}^i \left(\frac{v_j^i - v_{j-1}^i}{h_j}\right) + 2We\xi v_{j-1/2}^i \left(\frac{v_j^i - v_{j-1}^i}{h_j}\right) \\
&-2We\xi\gamma^* s_{j-1/2}^i v_{j-1/2}^i \left(\frac{v_j^i - v_{j-1}^i}{h_j}\right) - We\xi\gamma^* t_{j-1/2}^i \left(v_{j-1/2}^i\right)^2 \\
&-\gamma^*\left(t_{j-1/2}^i v_{j-1/2}^i\right) + (1+\alpha)\left(f_{j-1/2}^i v_{j-1/2}^i\right) - (1+\alpha)\left(u_{j-1/2}^i\right)^2 \\
&-(M_a)u_{j-1/2}^i + \alpha v_{j-1/2}^{i-1} f_{j-1/2}^i - \alpha f_{j-1/2}^{i-1} v_{j-1/2}^i + B\left(s_{j-1/2}^i - N_r g_{j-1/2}^i\right) \\
&= -\begin{bmatrix}
\left(\frac{v_j^i - v_{j-1}^i}{h_j}\right) - \gamma^* s_{j-1/2}^i \left(\frac{v_j^i - v_{j-1}^i}{h_j}\right) + 2We\xi v_{j-1/2}^i \left(\frac{v_j^i - v_{j-1}^i}{h_j}\right) \\
-2We\xi\gamma^* s_{j-1/2}^i v_{j-1/2}^i \left(\frac{v_j^i - v_{j-1}^i}{h_j}\right) - We\xi\gamma^* t_{j-1/2}^i \left(v_{j-1/2}^i\right)^2 \\
-\gamma^*\left(t_{j-1/2}^i v_{j-1/2}^i\right) + (1-\alpha)\left(f_{j-1/2}^{i-1} v_{j-1/2}^{i-1}\right) + (\alpha - 1) \\
\left(u_{j-1/2}^{i-1}\right)^2 + B\left(s_{j-1/2}^{i-1} - N_r g_{j-1/2}^{i-1}\right) - (M_a)u_{j-1/2}^{i-1}
\end{bmatrix}
\end{aligned}\right\} \quad (27)$$

$$\left.\begin{aligned}
&\frac{1}{\Pr}\left[1 + \frac{4}{3R_a}\right]\left(\frac{t_j^i - t_{j-1}^i}{h_j}\right) + \frac{\delta^*}{\Pr} s_{j-1/2}^i \left(\frac{t_j^i - t_{j-1}^i}{h_j}\right) \\
&+\frac{\delta^*}{\Pr}\left(t_{j-1/2}^i\right)^2 + N_B\left(t_{j-1/2}^i p_{j-1/2}^i\right) + N_T\left(t_{j-1/2}^i\right)^2 \\
&+D_u\left(\frac{p_j^i - p_{j-1}^i}{h_j}\right) - \alpha u_{j-1/2}^{i-1} s_{j-1/2}^i - \alpha f_{j-1/2}^{i-1} t_{j-1/2}^i \\
&+\alpha t_{j-1/2}^{i-1} f_{j-1/2}^i + (1+\alpha)\left(f_{j-1/2}^i t_{j-1/2}^i\right) \\
&-\alpha\left(u_{j-1/2}^i s_{j-1/2}^i\right) + \alpha s_{j-1/2}^{i-1} u_{j-1/2}^i \\
&= -\begin{bmatrix}
\frac{1}{\Pr}\left[1 + \frac{4}{3R_a}\right]\left(\frac{t_j^i - t_{j-1}^i}{h_j}\right) + \frac{\delta^*}{\Pr} s_{j-1/2}^i \left(\frac{t_j^i - t_{j-1}^i}{h_j}\right) \\
+\frac{\delta^*}{\Pr}\left(t_{j-1/2}^i\right)^2 + N_B\left(t_{j-1/2}^i p_{j-1/2}^i\right) \\
+N_T\left(t_{j-1/2}^i\right)^2 + D_u\left(\frac{p_j^i - p_{j-1}^i}{h_j}\right) \\
+(1-\alpha)\left(f_{j-1/2}^{i-1} t_{j-1/2}^{i-1}\right) + \alpha\left(u_{j-1/2}^{i-1} s_{j-1/2}^{i-1}\right)
\end{bmatrix}
\end{aligned}\right\} \quad (28)$$

$$\left.\begin{aligned}&\frac{1}{Sc}\left(\frac{p_j^i-p_{j-1}^i}{h_j}\right)+\frac{1}{Sc}\left(\frac{N_T}{N_B}\right)\left(\frac{t_j^i-t_{j-1}^i}{h_j}\right)+S_r\left(\frac{t_j^i-t_{j-1}^i}{h_j}\right)\\&+(1+\alpha)\left(f_{j-1/2}^i p_{j-1/2}^i\right)-\alpha\left(u_{j-1/2}^i g_{j-1/2}^i\right)+\alpha g_{j-1/2}^{i-1}u_{j-1/2}^i\\&-\alpha u_{j-1/2}^{i-1}g_{j-1/2}^i-\alpha f_{j-1/2}^{i-1}p_{j-1/2}^i+\alpha p_{j-1/2}^{i-1}f_{j-1/2}^i\\&=-\left[\begin{aligned}&\frac{1}{Sc}\left(\frac{p_j^i-p_{j-1}^i}{h_j}\right)+\frac{1}{Sc}\left(\frac{N_T}{N_B}\right)\left(\frac{t_j^i-t_{j-1}^i}{h_j}\right)+S_r\left(\frac{t_j^i-t_{j-1}^i}{h_j}\right)\\&+(1-\alpha)\left(f_{j-1/2}^{i-1}p_{j-1/2}^{i-1}\right)+\alpha\left(u_{j-1/2}^{i-1}g_{j-1/2}^{i-1}\right)\end{aligned}\right]\end{aligned}\right\}\tag{29}$$

where $\alpha=\frac{\xi^{n-1/2}}{k_n}, B=\frac{\sin\left(\xi^{n-1/2}\right)}{\xi^{n-1/2}}$

The boundary conditions become:

$$f_0^i=u_0^i=0,\ s_0^i=1,\ g_0^i=1,\ u_J^i=0,\ s_J^i=0,\ g_J^i=0\tag{30}$$

Step 3:

The unknowns $\left(f_j^i,\ u_j^i,\ v_j^i,\ g_j^i,\ p_j^i,\ s_j^i,\ t_j^i\right)$ are calculated with the help of following knowns $f_j^{i-1},\ u_j^{i-1},\ v_j^{i-1},\ g_j^{i-1}, p_j^{i-1},\ s_j^{i-1},\ t_j^{i-1}$ where $0\leq \mathrm{j}\leq \mathrm{J}$ and $\left(f_j^i,\ u_j^i,\ v_j^i,\ g_j^i,\ p_j^i,\ s_j^i,\ t_j^i\right)\equiv\left(f_j,\ u_j,\ v_j,\ g_j,\ p_j,\ s_j,\ t_j\right)$.

The set of central difference equations are expressed as follows:

$$\frac{u_j+u_{j-1}}{2}=\frac{f_j-f_{j-1}}{h_j},\tag{31}$$

$$\frac{v_j+v_{j-1}}{2}=\frac{u_j-u_{j-1}}{h_j},\tag{32}$$

$$\frac{t_j+t_{j-1}}{2}=\frac{s_j-s_{j-1}}{h_j},\tag{33}$$

$$\frac{p_j+p_{j-1}}{2}=\frac{g_j-g_{j-1}}{h_j},\tag{34}$$

$$\left.\begin{aligned}&(v_j-v_{j-1})-\frac{\gamma^*}{2}(s_j+s_{j-1})(v_j-v_{j-1})+We\xi(v_j+v_{j-1})(v_j-v_{j-1})\\&-\frac{We\xi\gamma^*}{2}(s_j+s_{j-1})(v_j+v_{j-1})(v_j-v_{j-1})-\frac{We\xi h_j\gamma^*}{8}(t_j+t_{j-1})\\&(v_j+v_{j-1})^2+\frac{(1+\alpha)h_j}{4}\left[\left(f_j+f_{j-1}\right)(v_j+v_{j-1})\right]-\frac{h_j}{4}(1+\alpha)\\&(u_j+u_{j-1})^2-\frac{\gamma^*}{4}h_j(v_j+v_{j-1})(t_j+t_{j-1})-\frac{h_j}{2}(M_a)(u_j+u_{j-1})\\&+\frac{\alpha h_j}{2}v_{j-1/2}^{i-1}\left(f_j+f_{j-1}\right)-\frac{\alpha h_j}{2}f_{j-1/2}^{i-1}(v_j+v_{j-1})\\&+\frac{Bh_j}{2}\left[s_j+s_{j-1}-N_r(g_j+g_{j-1})\right]=[E_1]_{j-1/2}^{i-1}\end{aligned}\right\}\tag{35}$$

$$\left.\begin{aligned}
&\frac{1}{\mathrm{Pr}}\left[1+\frac{4}{3R_a}\right](t_j-t_{j-1})+\frac{\delta^*}{2\mathrm{Pr}}(s_j+s_{j-1})(t_j-t_{j-1})\\
&+\frac{\delta^*}{4\mathrm{Pr}}h_j(t_j+t_{j-1})^2+\frac{N_B}{4}h_j(t_j+t_{j-1})(p_j+p_{j-1})\\
&+\frac{N_T}{4}h_j(t_j+t_{j-1})^2+D_u(p_j-p_{j-1})+\frac{(1+\alpha)h_j}{4}(f_j+f_{j-1})\\
&(t_j+t_{j-1})-\frac{\alpha h_j}{4}[(u_j+u_{j-1})(s_j+s_{j-1})]\\
&+\frac{\alpha h_j}{2}s^{i-1}_{j-1/2}(u_j+u_{j-1})-\frac{\alpha h_j}{2}u^{i-1}_{j-1/2}(s_j+s_{j-1})\\
&-\frac{\alpha h_j}{2}f^{i-1}_{j-1/2}(t_j+t_{j-1})+\frac{\alpha h_j}{2}t^{i-1}_{j-1/2}(f_j+f_{j-1})=[E_2]^{i-1}_{j-1/2}
\end{aligned}\right\} \quad (36)$$

$$\left.\begin{aligned}
&\frac{1}{Sc}(p_j-p_{j-1})+\frac{1}{Sc}\frac{N_T}{N_B}(t_j-t_{j-1})+S_r(t_j-t_{j-1})\\
&+\frac{(1+\alpha)h_j}{4}[(f_j+f_{j-1})(p_j+p_{j-1})]-\frac{\alpha h_j}{4}[(u_j+u_{j-1})(g_j+g_{j-1})]\\
&+\frac{\alpha h_j}{2}g^{i-1}_{j-1/2}(u_j+u_{j-1})-\frac{\alpha h_j}{2}u^{i-1}_{j-1/2}(g_j+g_{j-1})\\
&-\frac{\alpha h_j}{2}f^{i-1}_{j-1/2}(p_j+p_{j-1})+\frac{\alpha h_j}{2}p^{i-1}_{j-1/2}(f_j+f_{j-1})=[E_3]^{i-1}_{j-1/2}
\end{aligned}\right\} \quad (37)$$

Here $[E_1]^{i-1}_{j-1/2}$, $[E_2]^{i-1}_{j-1/2}$ and $[E_3]^{i-1}_{j-1/2}$ are the known quantities:

$$[E_1]^{i-1}_{j-1/2}=-h_j\begin{bmatrix}
\left(\frac{v_j-v_{j-1}}{h_j}\right)-\gamma^* s_{j-1/2}\left(\frac{v_j-v_{j-1}}{h_j}\right)+2We\,\xi v_{j-1/2}\\
\left(\frac{v_j-v_{j-1}}{h_j}\right)-2We\,\xi\,\gamma^* s_{j-1/2}v_{j-1/2}\left(\frac{v_j-v_{j-1}}{h_j}\right)\\
-We\,\xi\,\gamma^* t_{j-1/2}(v_{j-1/2})^2-\gamma^*(t_{j-1/2}v_{j-1/2})\\
+(1-\alpha)\left(f_{j-1/2}v_{j-1/2}\right)+(\alpha-1)(u_{j-1/2})^2\\
+B\left(s_{j-1/2}-N_r g_{j-1/2}\right)-(M_a)u_{j-1/2}
\end{bmatrix}$$

$$[E_2]^{i-1}_{j-1/2}=-h_j\begin{bmatrix}
\frac{1}{\mathrm{Pr}}\left[1+\frac{4}{3R_a}\right]\left(\frac{t_j-t_{j-1}}{h_j}\right)+\frac{\delta^*}{\mathrm{Pr}}s_{j-1/2}\left(\frac{t_j-t_{j-1}}{h_j}\right)\\
+\frac{\delta^*}{\mathrm{Pr}}(t_{j-1/2})^2+N_B(t_{j-1/2}p_{j-1/2})\\
+N_T(t_{j-1/2})^2+D_u\left(\frac{p_j-p_{j-1}}{h_j}\right)\\
+(1-\alpha)\left(f_{j-1/2}t_{j-1/2}\right)+\alpha(u_{j-1/2}s_{j-1/2})
\end{bmatrix}$$

$$[E_3]_{j-1/2}^{i-1} = -h_j \begin{bmatrix} \frac{1}{Sc}\left(\frac{p_j - p_{j-1}}{h_j}\right) + \frac{1}{Sc}\left(\frac{N_T}{N_B}\right)\left(\frac{t_j - t_{j-1}}{h_j}\right) + \\ S_r\left(\frac{t_j - t_{j-1}}{h_j}\right) + (1-\alpha)\left(f_{j-1/2}p_{j-1/2}\right) \\ +\alpha\left(u_{j-1/2}g_{j-1/2}\right) \end{bmatrix}$$

Linearization and block elimination processes of Keller Box Method scheme is provided in the Appendix section.

In the present problem, the maximum values of ξ and η are considered as 1 and 30, respectively. The difference between the spatial nodes are taken as 0.05 in both directions for convergence of the solution. It is noteworthy to mention that the pseudoplastic nanofluid boundary layer regime is meshed with (20×600) grid points. To increase the accuracy of the present solution, the convergence criterion has been fixed as 10^{-6} at all grid points. Comparison results of Nu^* for various values of streamwise coordinate, ξ, are provided in Table 1. It is evident that the current Keller box solutions achieve a very good agreement with the results obtained by Merkin (1977), Yih (2000) and Prasad *et al.* (2019) when nanoscale and other effects are neglected to reduce the current boundary value problem to exactly that considered by these earlier studies with exactly the same data prescribed. It is witnessed that the obtained Keller box code is therefore justifiably very high. Tables 2, 3 and 4 documents the Keller box solutions for skin friction factor, rates of heat and mass transfer with diverse values in key parameters. These tables provide a useful benchmark for future researchers to validate alternative numerical computations with supplementary multi-physical effects. Figure 2 illustrates the Keller box numerical methodology, boundary layer mesh and Keller box discretization process.

Table 1.
Comparison result of Nu^* for various values of ξ with $P_r = 0.71$, $R_a \to \infty$, $M_a = 0.5$, $S_c = 0.6$, $We = N_r = \gamma^* = \delta^* = N_B = N_T = D_u = S_r = 0$

ξ	$Nu^{*} = -\theta'(\xi,0)$			
	Merkin (1977)	Yih (2000)	Prasad *et al.* (2019)	Present
0.0	0.4212	0.4214	0.4211	0.4211
0.2	0.4204	0.4207	0.4206	0.4206
0.4	0.4182	0.4184	0.4185	0.4185
0.6	0.4145	0.4147	0.4146	0.4146
0.8	0.4093	0.4096	0.4095	0.4095
1.0	0.4025	0.4030	0.4027	0.4027
1.2	0.3942	0.3950	0.3947	0.3947
1.4	0.3843	0.3854	0.3852	0.3852
1.6	0.3727	0.3740	0.3735	0.3735
1.8	0.3594	0.3608	0.3598	0.3598
2.0	0.3443	0.3457	0.3448	0.3448
2.2	0.3270	0.3283	0.3280	0.3280
2.4	0.3073	0.3086	0.3076	0.3076
2.6	0.2847	0.2860	0.2852	0.2852
2.8	0.2581	0.2595	0.2592	0.2592
3.0	0.2252	0.2267	0.2255	0.2255
π	0.1963	0.1962	0.1961	0.1961

Physical parameters	Values	Physical quantities	ξ 0	0.5	1	1.5	2	2.5	CPU time(s.)
		C_f^*	0	0.2284	0.4048	0.4779	0.4482	0.2708	
	0	Nu^*	0.5761	0.5590	0.5271	0.4757	0.4055	0.3013	8.365484
		Sh^*	0.1523	0.1479	0.1395	0.1261	0.1078	0.0804	
		C_f^*	0	0.2006	0.3612	0.4178	0.4047	0.2421	
γ^*	0.2	Nu^*	0.5839	0.5645	0.5338	0.4802	0.4118	0.3056	8.061629
		Sh^*	0.1542	0.1492	0.1411	0.1272	0.1093	0.0814	
		C_f^*	0	0.1667	0.3059	0.3479	0.3433	0.2156	
	0.4	Nu^*	0.5933	0.5701	0.5414	0.4850	0.4186	0.3118	9.043056
		Sh^*	0.1564	0.1504	0.1430	0.1283	0.1109	0.0830	
		C_f^*	0	0.1466	0.2719	0.3077	0.3046	0.1996	
	0.6	Nu^*	0.5987	0.5728	0.5455	0.4877	0.4221	0.3158	12.654024
		Sh^*	0.1577	0.1510	0.1439	0.1289	0.1118	0.0839	
		C_f^*	0	0.1962	0.3529	0.4081	0.3948	0.2354	
	0	Nu^*	0.5469	0.5286	0.4996	0.4490	0.3844	0.2839	8.193623
		Sh^*	0.1400	0.1355	0.1281	0.1154	0.0989	0.0735	
		C_f^*	0	0.2006	0.3612	0.4178	0.4047	0.2421	
δ^*	0.5	Nu^*	0.5839	0.5645	0.5338	0.4802	0.4118	0.3056	8.239927
		Sh^*	0.1542	0.1492	0.1411	0.1272	0.1093	0.0814	
		C_f^*	0	0.2045	0.3683	0.4261	0.4132	0.2480	
	1.0	Nu^*	0.6198	0.5993	0.5669	0.5104	0.4384	0.3268	8.099395
		Sh^*	0.1657	0.1603	0.1518	0.1368	0.1178	0.0880	
		C_f^*	0	0.2077	0.3744	0.4333	0.4206	0.2532	
	1.5	Nu^*	0.6546	0.6332	0.5991	0.5398	0.4642	0.3474	9.210965
		Sh^*	0.1753	0.1695	0.1606	0.1448	0.1249	0.0935	

Table 2.
Impacts of γ^* and δ^* on local skin friction coefficient (C_f^*), dimensionless local rate of heat transfer (Nu^*) and dimensionless local rate of mass transfer (Sh^*) for various values of ξ

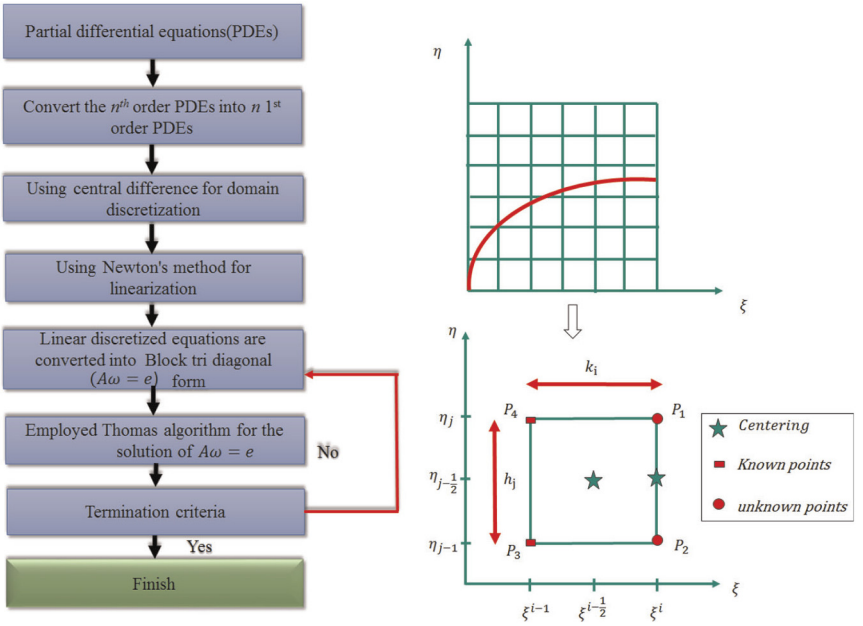

Figure 2.
Solution approach by computer, boundary layer mesh and Keller box cell

4. Results and discussion

The current section is aimed to visualize the influence of emerging parameters on velocity (f'), temperature (θ), concentration (ϕ), skin friction factor (C_f^*), wall heat transfer rate (Nu^*) and wall nanoparticle mass transfer rate (Sh^*). The parameters varied and their values are: Weissenberg number (We = 0.0,0.5,1.0,1.5), magnetic field (M_a = 0.0,0.5,1.0,1.5), variable viscosity parameter (γ^* = 0.0,0.2,0.4,0.6), variable thermal conductivity parameter (δ^* = 0.0,0.5,1.0,1.5), Brownian motion (N_B = 0.2,0.4,0.6,0.8), thermophoresis (N_T = 0.01,0.1,0.3,1.5), radiation (R_a = 0.1,0.3,0.5,0.8), Soret number (S_r = 0.4,0.2,0.1,0.075) and Dufour number (D_u = 0.15,0.3,0.6,0.8). All used data in the simulations is based on practically viable nano-materials processing systems which is extracted from Das *et al.* (2007) and Jaluria (2013). Figures 3–22 depict the variation in momentum, heat transfer and nanoparticle concentration characteristics and consistently smooth profiles are achieved in the free stream, testifying to the prescription of an adequately larger infinity boundary condition. A further novelty in the current study is that Figures 23–25 have been included to visualize the 3D contour distributions and Figures 26–28 have been provided to illustrate the streamline, isothermal and iso-concentration distributions. This color contoured visualization has invariably been omitted in the majority of Keller box numerical studies.

The impact of magnetic field (M_a) on velocity (f'), temperature (θ) and nanoparticle concentration (ϕ) are depicted in Figures 3–5. In an electrically conducting fluid (e.g. magnetic nano-polymer), the magnetic field applied in the transverse direction creates an orthogonal hydromagnetic retarding force (Lorentz force) which resists the fluid motion. The magnitude of Lorentz force increases with an increase in the strength of the magnetic field B_0. The implication is that regulation in coating flow of the magnetic nano-polymer is achieved successfully via a boost in radial magnetic field which permits more homogenous distribution of the nano-polymer over the cylinder periphery. The classical velocity overshoot is arising in close proximity to the wall (cylinder surface), and it is progressively suppressed with greater values of M_a. Maximum acceleration and thickest boundary layer thickness corresponds to the electrically non-conducting case (M_a = 0). Although a slight

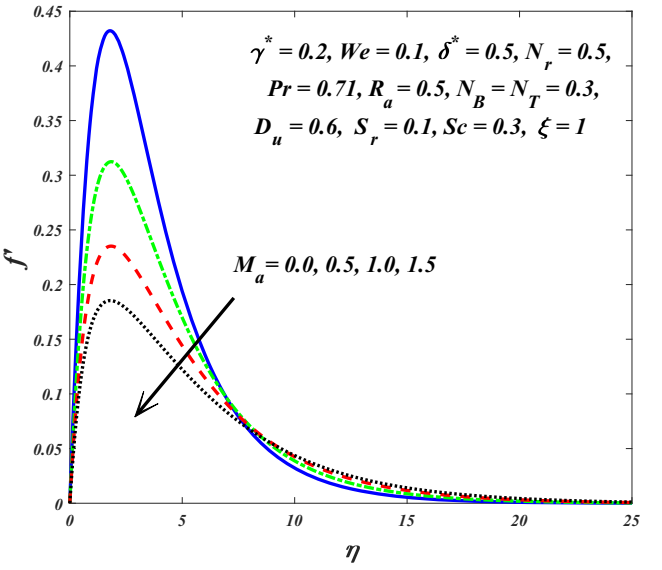

Figure 3.
f' for uplifting values of M_a

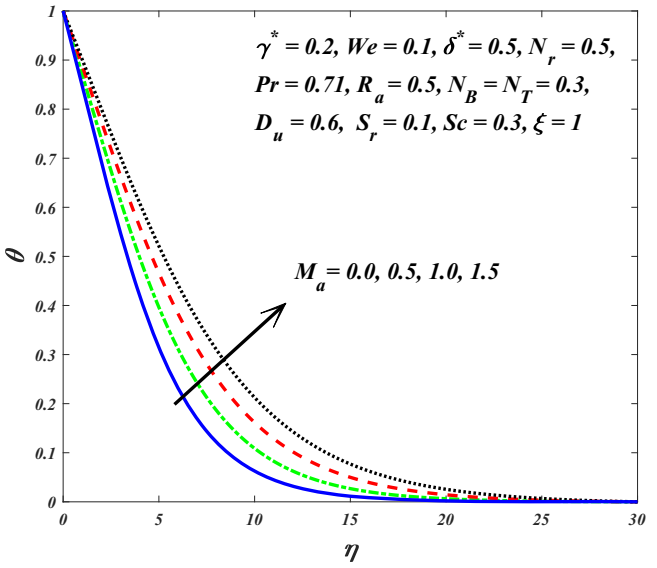

Figure 4.
θ for uplifting values of M_a

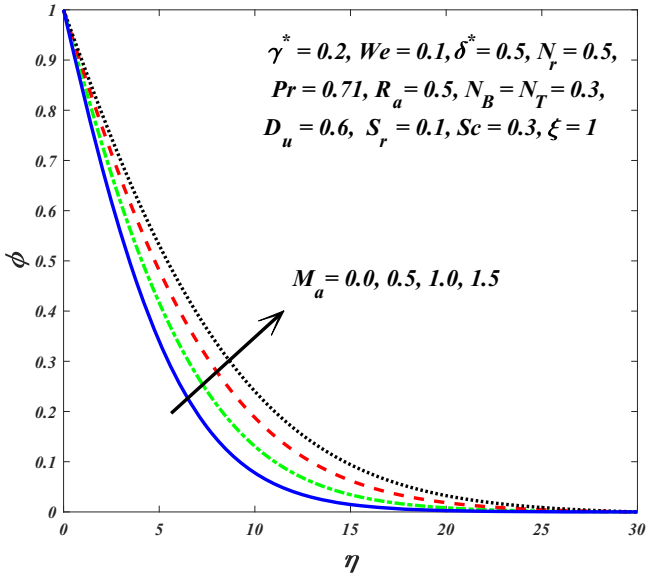

Figure 5.
ϕ for uplifting values of M_a

switch in the effect of magnetic field on velocity distribution is generated further from the cylinder surface (approaching the free stream), the dominant effect is retardation. However, back flow is never instigated because velocities are consistently positive indicating that even at relatively strong magnetic field (M_a = 1.5), flow separation is avoided. The evolutions in temperature and nano-particle concentration with magnetic field are displayed

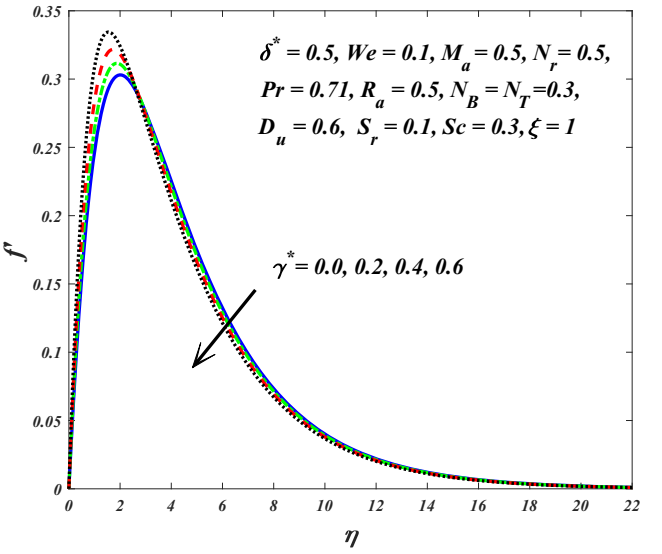

Figure 6.
f' for uplifting values of γ^*

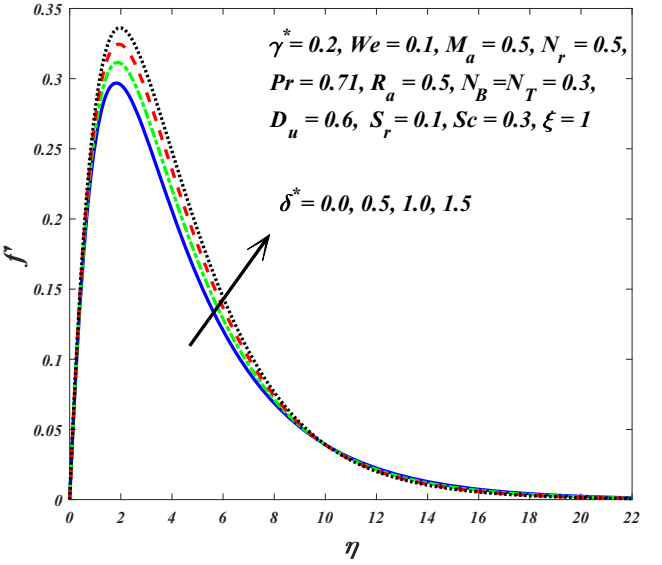

Figure 7.
f' for uplifting values of δ^*

in Figures 4 and 5, respectively. Strengthening the magnetic field results in enhancing the Lorentz force which necessitates greater work expenditure by the nanofluid in dragging against the action of the magnetic field. This excess work is dissipated as thermal energy which heats the coating regime and elevates thermal boundary layer thickness. A consistently monotonic decay in the fluid temperature from the cylinder surface to the free stream is computed (Figure 4). Simultaneously the nanoparticle diffusion is assisted in the

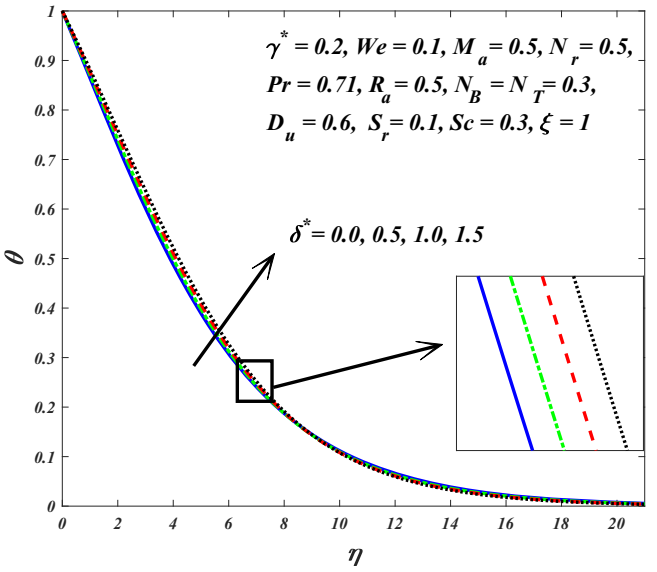

Figure 8.
θ for uplifting values of δ^*

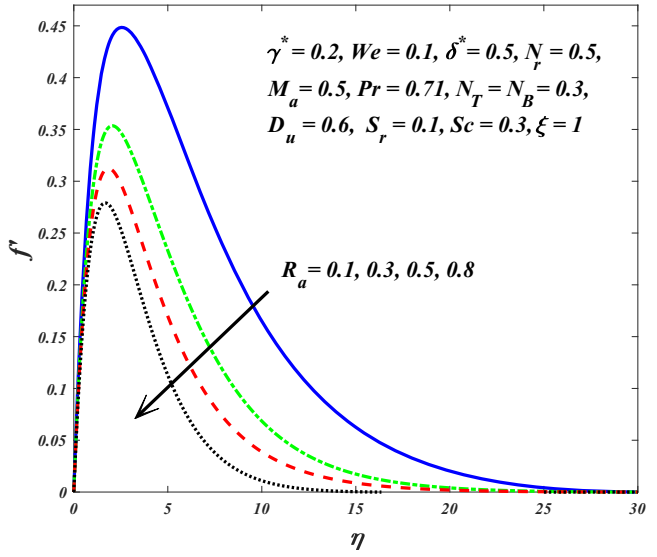

Figure 9.
f' for uplifting values of R_a

boundary layer, i.e. nanoparticle concentration magnitudes (Figure 5) are boosted for strengthening the magnetic field. Magnetic field therefore has the dual benefit of flow control and mobilization of more homogenous migration of nanoparticles; however, it leads to temperature and concentration elevation.

The response in velocity distribution to variable viscosity parameter (γ^*) is given in Figure 6. γ^* takes positive values to characterize the liquids such as water, crude oil and

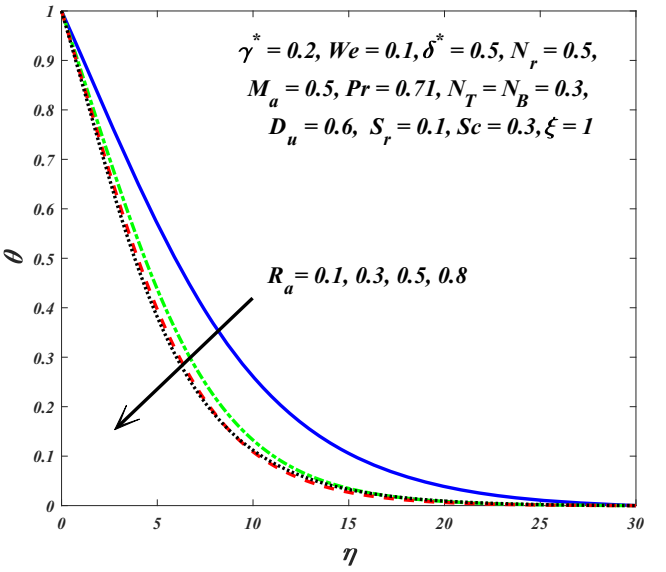

Figure 10.
θ for uplifting values of R_a

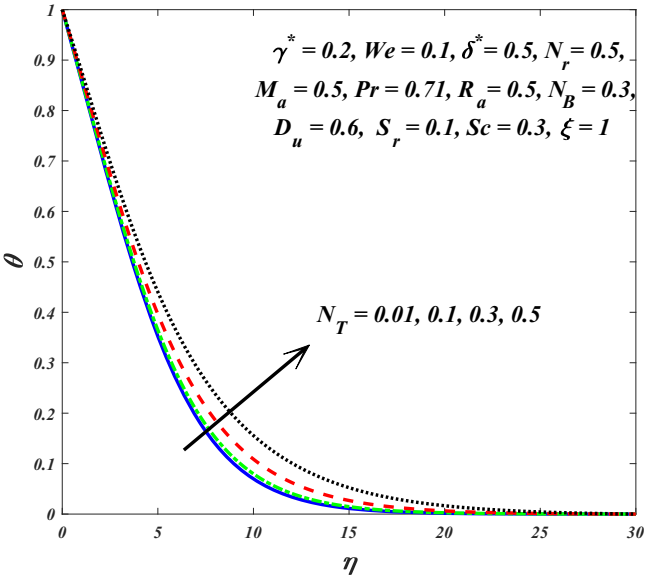

Figure 11.
θ for uplifting values of N_T

benzene, whereas it takes negative values to represent the gases such as air, methane and helium. It is apparent that higher values of variable viscosity parameter initially slightly increases the Williamson fluid velocity near the cylinder surface (wall); however, the dominant effect is a deceleration which extends through the majority of the boundary layer region, and it is attributable to the reduction in momentum diffusion. A similar response has

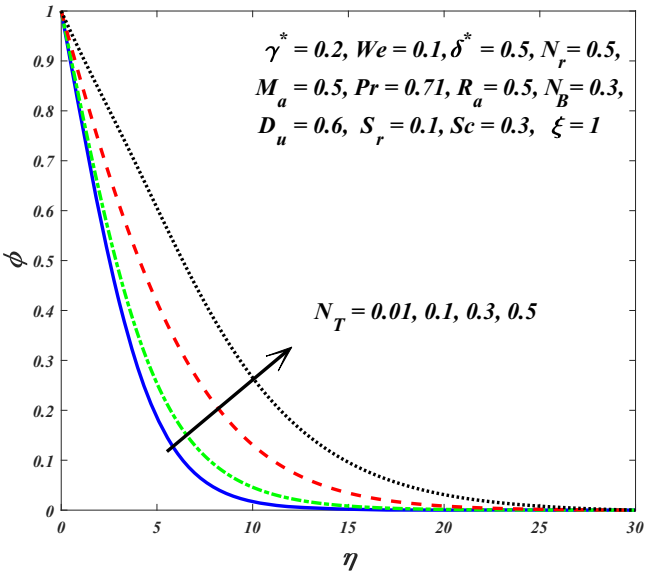

Figure 12.
ϕ for uplifting values of N_T

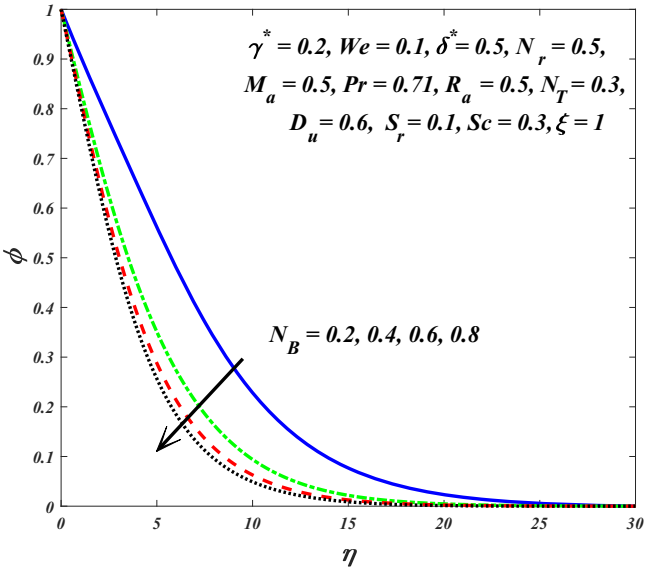

Figure 13.
ϕ for uplifting values of N_B

been reported by Kafoussias and Williams (1995) and Nasrin and Alim (2009), among many other studies. Figures 7 and 8 exhibit the influence of variable thermal conductivity parameter δ^* on nanofluid velocity and temperature. It is evident from these figures that both characteristics manifest an elevation with higher values of δ^*. This parameter features in the augmented thermal diffusion term, $(1 + \delta^*\theta)\theta''/\mathrm{Pr}$ in the energy equation (11) and

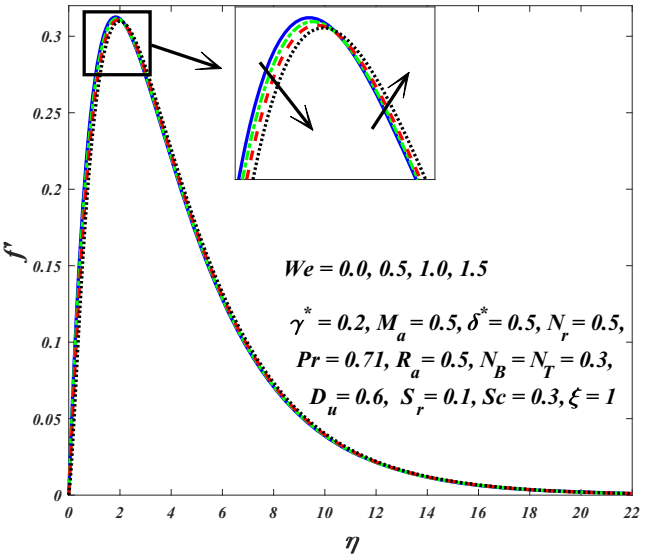

Figure 14.
f' for uplifting values of *We*

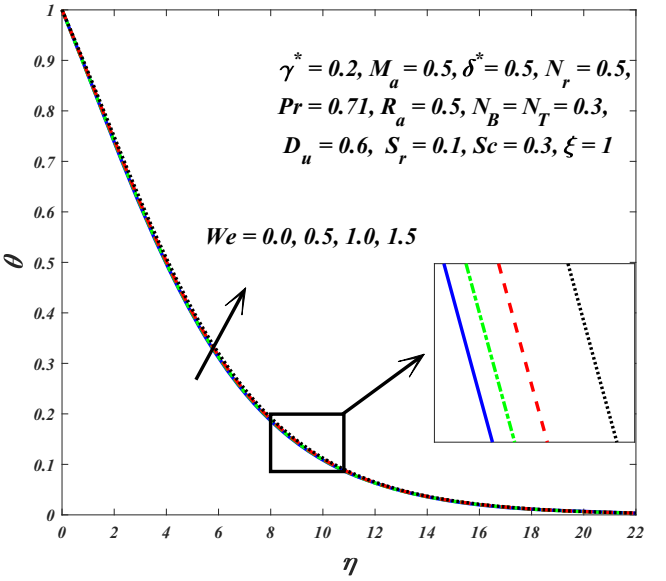

Figure 15.
θ for uplifting values of *We*

accentuates heat transfer inside the nanofluid. Higher values of thermal conductivity variation parameter intensify thermal conduction which assists in thermal diffusion and momentum diffusion. This results in a slight accentuation in hydrodynamic and thermal boundary layer thicknesses. Evidently, the inclusion of thermal conductivity variation produces results which more accurately predict the velocity and temperature magnitudes. Absence of this parameter (δ^*=0) leads to an under-prediction in both quantities which

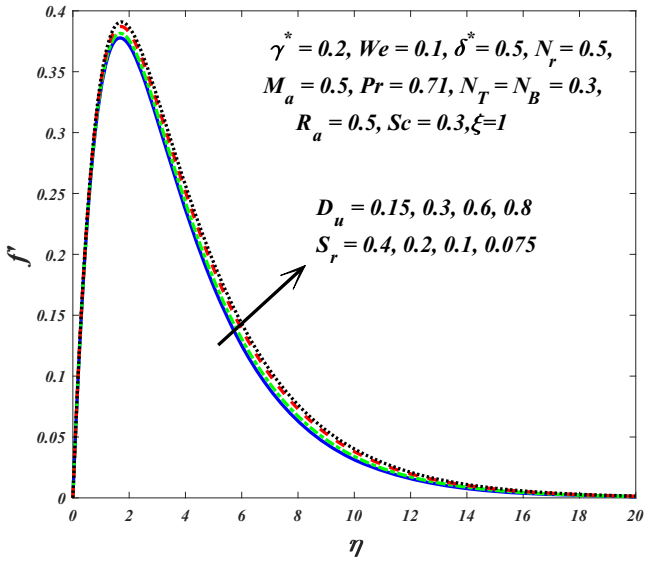

Figure 16.
f' for uplifting and decreasing values of D_u and S_r

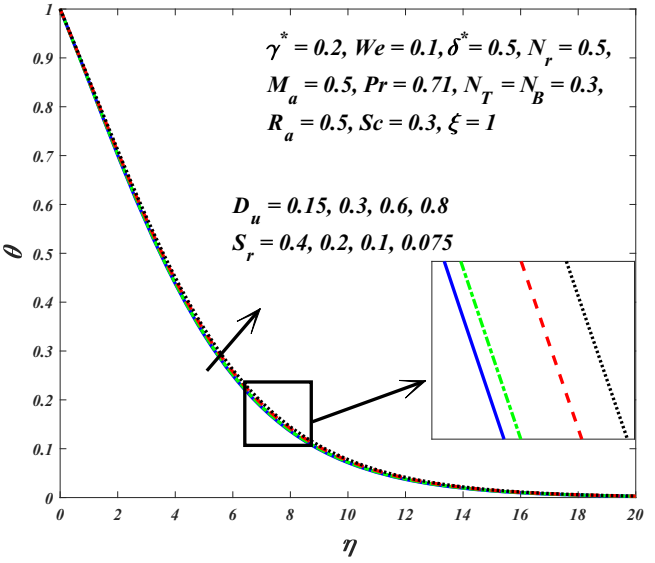

Figure 17.
θ for uplifting and decreasing values of D_u and S_r

results in lower momentum and lower thermal boundary layer thickness estimates, which are undesirable in manufacturing operations and can incur expenses, as noted by Jaluria (2013).

Figures 9 and 10 depict the influence of Rossleand conduction-radiation parameter (R_a) on fluid velocity and temperature profiles, respectively. Like the thermal conductivity variation parameter δ^*, the Rossleand conduction-radiation parameter $R_a = \frac{k_e k_{0f}}{4\sigma_B T_\infty^3}$ is an

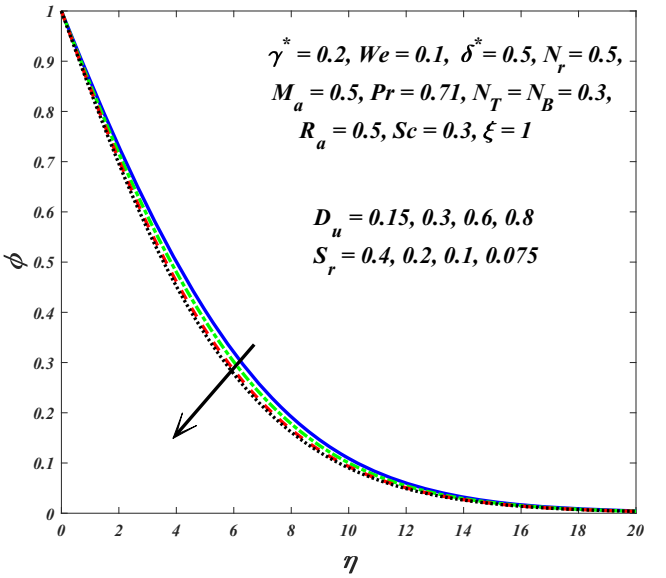

Figure 18.
ϕ for uplifting and decreasing values of D_u and S_r

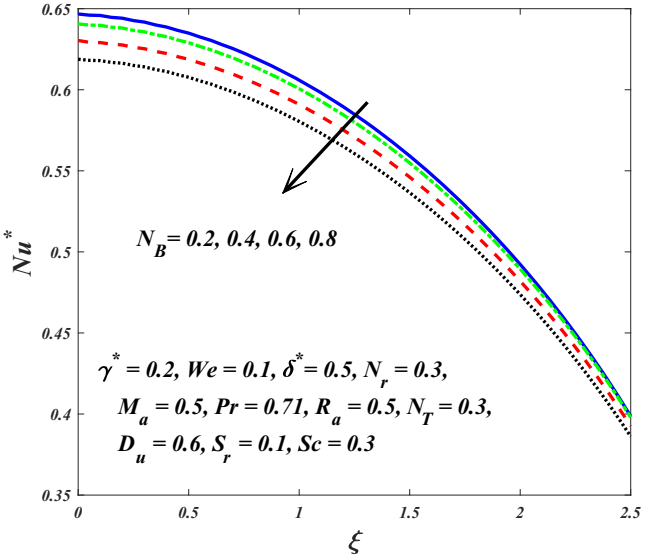

Figure 19.
Nu^* for uplifting values of N_B

additional feature in the thermal diffusion term, $(4/3\mathrm{Pr}R_a)\theta''$. Although the parameter exists in denominator, the contribution is still that of thermal conduction heat transfer relative to radiative heat transfer. As R_a increases, thermal conduction becomes progressively larger (for $R_a < 1$ it always dominates thermal radiation), and this causes the flow to decline (Figure 8). For higher values of R_a, more heat is transferred away from the geometry, and

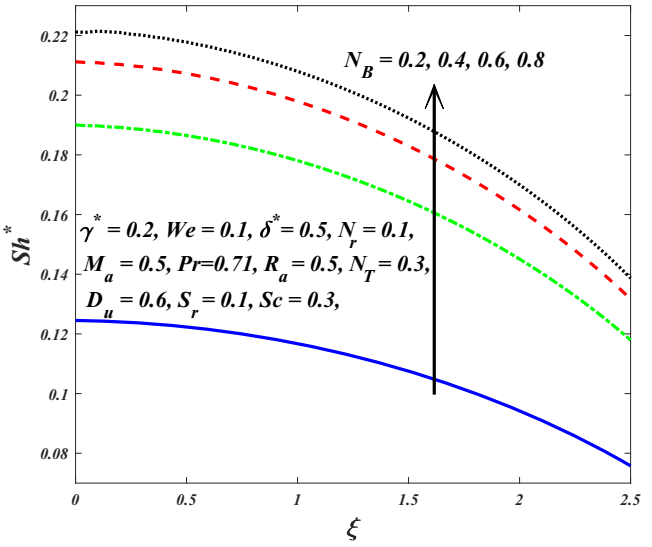

Figure 20.
Sh^* for uplifting values of N_B

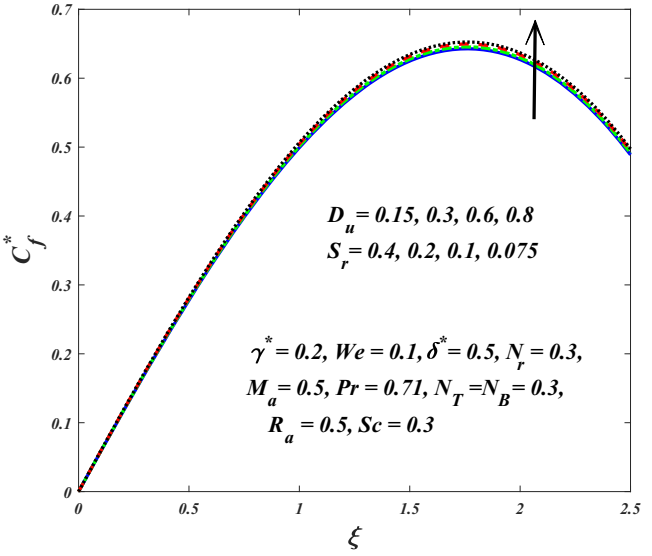

Figure 21.
C_f^* for uplifting and decreasing values of D_u and S_r

this leads to lower temperature and thinner thermal boundary layer thickness (Figure 9). It is noteworthy that the Rosseland model assumes that radiative equilibrium is sustained in the simulations, and the nanofluid is gray, and furthermore that the intensity is the black-body intensity at the nanofluid temperature. Implicit in this flux approximation is the requirement that the optical thickness exceeds three for reasonable accuracy as noted by Modest (1992) and later Beg *et al.* (2016). Optical thickness and absorption coefficient are dimensionless quantifications of how much a given medium (nanofluid) retards the passage

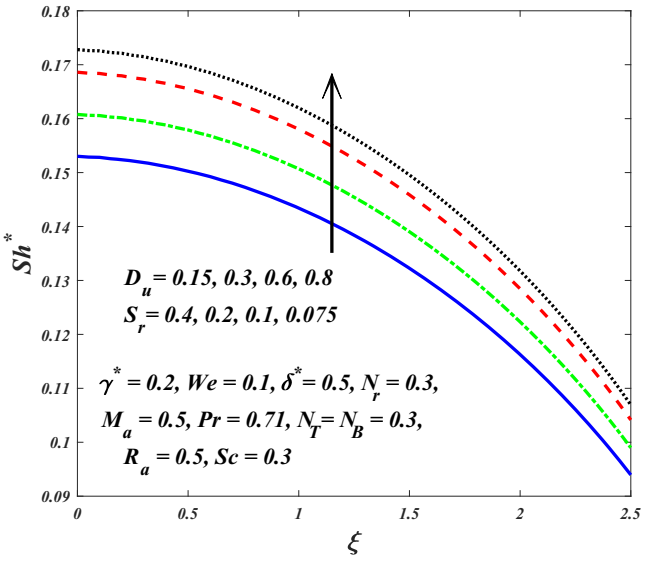

Figure 22.
Sh^* for uplifting and decreasing values of D_u and S_r

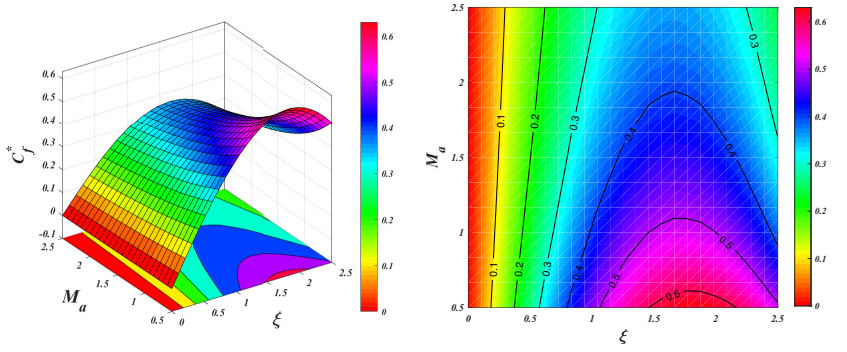

Figure 23.
Impact of M_a on C_f^*

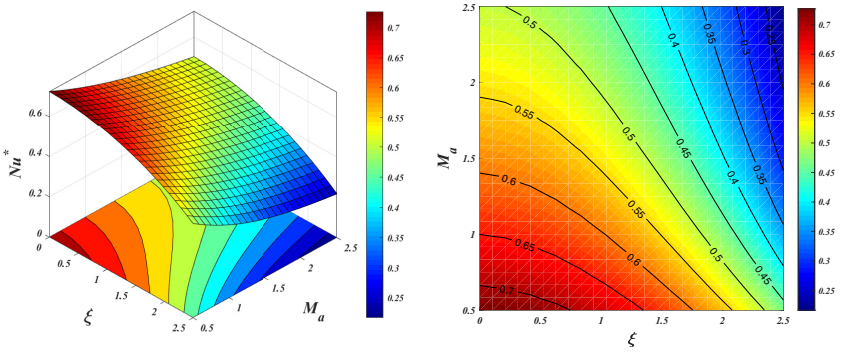

Figure 24.
Impact of M_a on Nu^*

of thermal radiation. Radiative intensity falls by an exponential factor when optical thickness is unity. Physically optical thickness will be a function of absorption coefficient (k_e), medium density and propagation distance. Although the flux model is much simpler than other algebraic approximations (e.g. P1 Traugott model), it does predict fairly accurately the influence of radiative flux.

Figure 11 illustrates the effect of thermophoresis (N_T) on nanofluid temperature distribution. In the phenomenon of thermophoresis, the heated nanoparticles are pushed from a hot surface to a cold area. Thermophoretic body force therefore mobilizes nanoparticle migration from the cylinder surface and encourages heat diffusion into the boundary layer away from the wall. This results in an elevation in nanofluid temperature and a concomitant increase in thermal boundary layer thickness. A similar pattern has been reported in many other studies including Raju and Sandeep (2016) and Prasad *et al.* (2019). The influence of thermophoresis on nanoparticle concentration profiles is illustrated in Figure 12. It is confirmed that thermophoretic body force promotes the transport of nanoparticles by moving the nanoparticles from the heated isothermal cylinder wall to the nanofluid boundary layer regime and therefore enhances nanoparticle concentration magnitudes. The amplification in magnitudes is considerably greater than temperatures because thermophoresis is essentially a species diffusion phenomenon which affects thermal field, as simulated in the quadratic temperature derivative term, $N_T(\theta')^2$ in the thermal boundary layer equation (11). A simultaneous enhancement in nanoparticle concentration boundary layer thickness is also induced.

The effect of Brownian motion parameter (N_B) on Williamson nanofluid concentration is exhibited in Figure 13. It is known that larger values of Brownian motion parameter N_B in the Buongiorno model correspond to smaller nanoparticle sizes and a reduction in ballistic collisions which diminish the nanoparticle concentration i.e. there is a depletion in the volume fraction. In the Buongiorno model, N_B arises in a coupled thermal-species diffusion term, also in the energy equation (11), viz, $N_B\theta'\phi'$. When this term is magnified, the species diffusion is reduced. A limitation of this model is that actual nanoparticle types, e.g. metallic oxides or carbon silicates cannot be simulated because a framework for their properties cannot be accommodated. This is achievable in the Tiwari–Das model, as noted by Beg *et al.* (2019b). However, the Tiwari–Das model does not feature a mechanism for species diffusion because it omits a concentration balance equation. A possible remedy to this dilemma is the fusion of both models and this is currently under investigation.

Figure 14 exhibits the modification in velocity profiles with Weissenberg rheological number. It is known that Weissenberg number is the ratio between the fluid stress

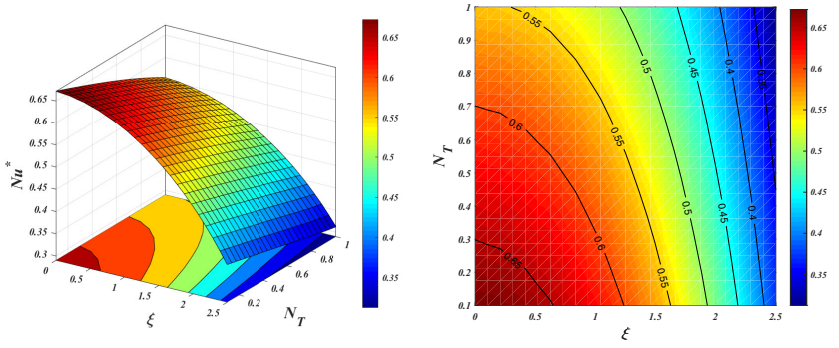

Figure 25.
Impact of N_T on Nu^*

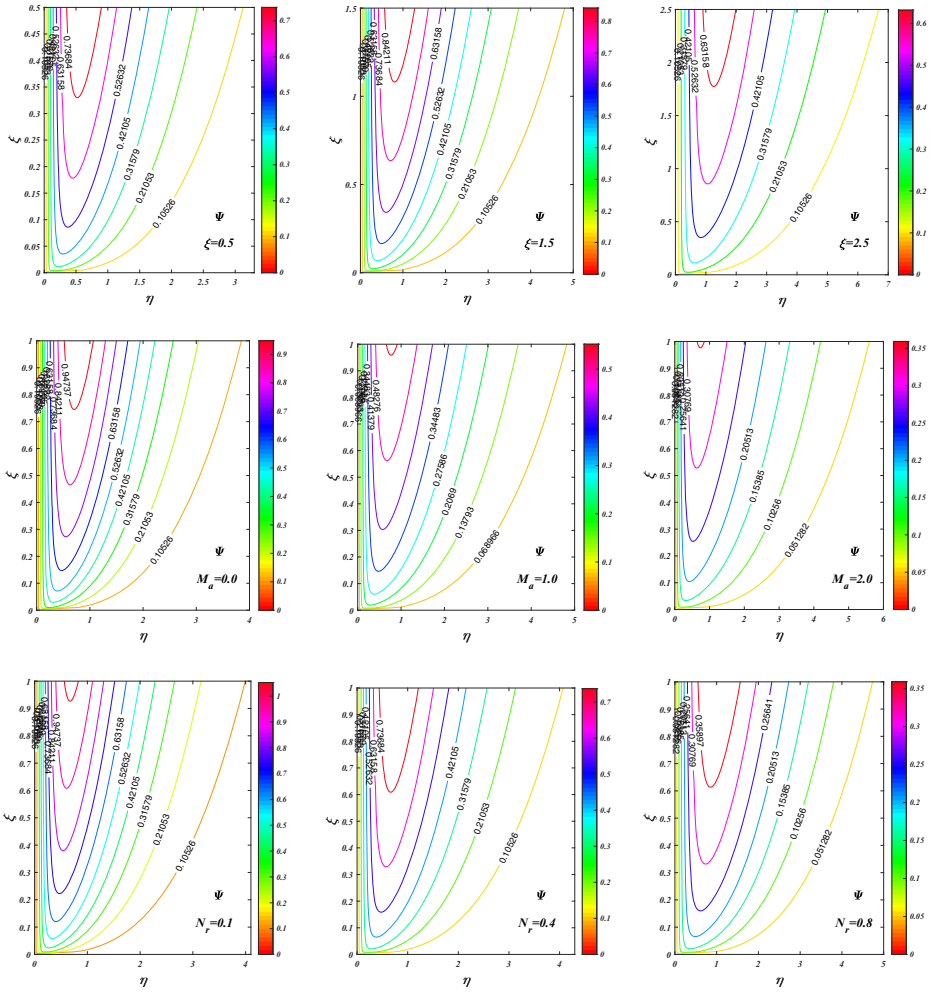

Figure 26.
Streamlines for uplifting values of ξ, M_a and N_r

relaxation time and specific process time. This parameter is a measure of the elastic force in a fluid to the viscous hydrodynamic force. It can be regarded as the product of shear rate and relaxation time and is generally obtained via scaling the evolution of the stress, based on a careful selection of shear or elongation rate, and the length-scale. Weissenberg number features strongly in the terms, $2We\xi(1 - \gamma^* \theta)f'''f' - We\xi\ \gamma^*\ (f'')^2\theta'$ in the momentum equation (10). A weak flow deceleration is induced near the cylinder surface, whereas further into the boundary layer, transverse to the cylinder, a weak acceleration is observed. The pseudoplastic fluid experiences strong tensile stresses near the wall which prohibit momentum diffusion. These forces are relaxed with greater distance from the wall (cylinder surface) and manifest in a slight enhancement in velocities. These findings are corroborated with other investigations including Malik *et al.* (2016). Figure 15 shows the influence of Weissenberg number on temperature profiles. Higher values of Weissenberg number enhance the fluid relaxation time, as a result, momentum diffusion is encouraged. Although

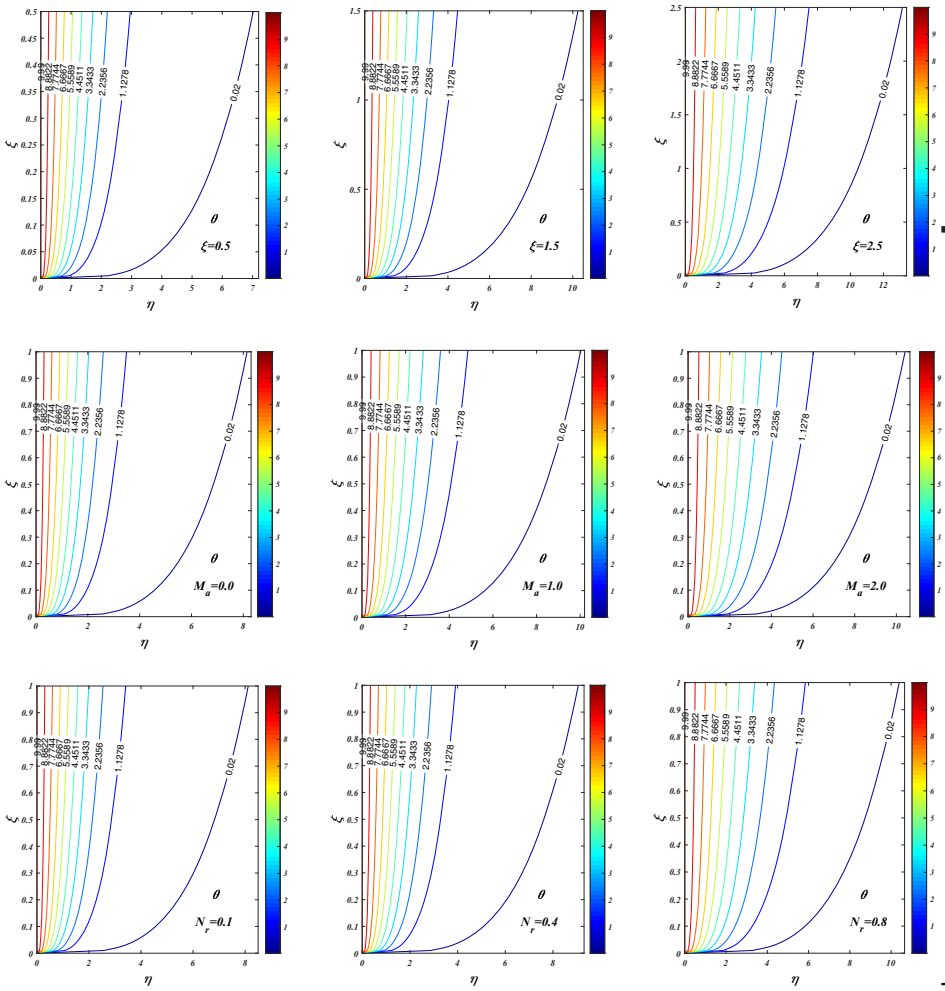

Figure 27.
Isotherms for uplifting values of ξ, M_a and N_r

We does not feature in the energy equation (11), the velocity–temperature coupling terms which include the convective terms, $\xi\left[f'\frac{\partial\theta}{\partial\xi}-\theta'\frac{\partial f}{\partial\xi}\right]$, and $f\theta'$ result in an indirect effect of elasticity on the temperature field. This results in a weak elevation in nanofluid temperature with an increase in Weissenberg number and a slight thickening in thermal boundary layer external to the cylinder.

Figures 16–18 are portrayed to display the influence of Soret and Dufour numbers on nanofluid velocity, temperature and nanoparticle concentration distributions, respectively. Williamson nanofluid velocity and temperature distributions (Figures 16 and 17) consistently increase with increment in Dufour number and simultaneous decrement in Soret number. The Dufour diffuso-thermal concentration gradient term, $D_u\theta''$ in the energy equation (11) clearly assists in thermal diffusion whereas the Soret thermo-diffusion term, $S_r\theta''$ in the nanoparticle concentration equation (12) opposes thermal diffusion. Effectively

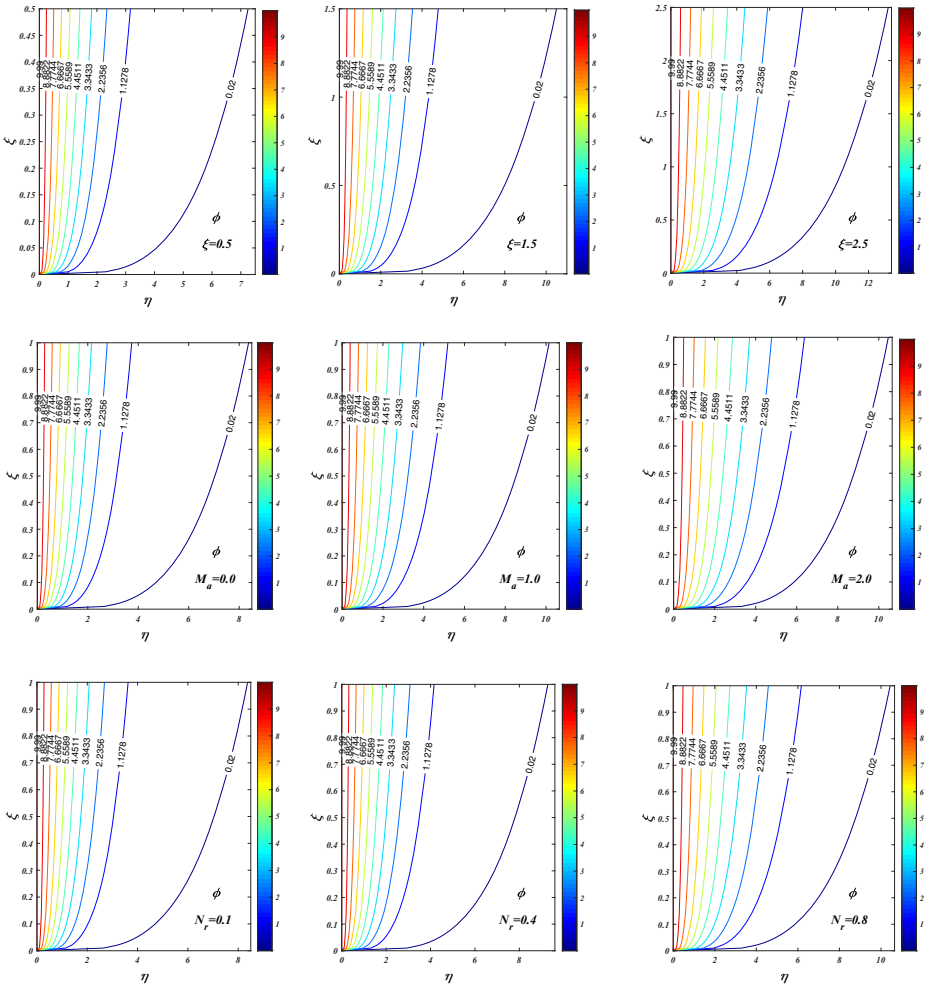

Figure 28.
Isoconcentrations for uplifting values of ξ, M_a and N_r

thermal boundary layer thickness is boosted with greater Du values and depleted with greater S_r values. The modification in velocity is via coupling of the energy and nanoparticle concentration equations to the momentum equation (10) in numerous terms, but notably the dual buoyancy (thermo-solutal) term, $\frac{\mathrm{Sin}\xi}{\xi}(\theta - N_r\phi)$. The contrary behavior is computed in Figure 18, wherein an increase in Dufour number with a reduction in Soret number is observed to depress nanoparticle concentration. Stronger Soret effect (thermo-diffusion) is therefore assistive to migration of nanoparticles, whereas stronger Dufour effect (diffuso-thermal) is inhibitive.

Figures 19 and 20 show the impact of Brownian motion parameter on Nusselt and Sherwood numbers at the cylinder surface. A substantial suppression in Nusselt number is induced with increasing values of Brownian motion, but the reverse behavior is exhibited (i.e. a strong elevation) in Sherwood numbers. In both plots, the maximum rates of heat and mass transfer at the wall are computed at $\xi = 0$ (lower stagnation point) and progressively

decrease with increasing streamwise coordinate, ξ. It is to be noted that greater Brownian motion clearly encourages heating in the nanofluid (elevation in temperature) by drawing heat away from the cylinder surface which leads to a plummet in Nusselt number. Conversely, higher Brownian motion effect (smaller nanoparticles) produces a reduction in nanoparticle concentration values in the nanofluid such that greater translocation of nanoparticles to the boundary (cylinder surface) is mobilized, which explains the considerable magnification in Sherwood number.

Figure 21 illustrates the influence of Soret and Dufour numbers on the skin friction factor, i.e. dimensionless shear stress at the cylinder surface. Skin friction factor vanishes at $\xi = 0$, a characteristic of stagnation point flow, i.e. the flow is brought to rest here, and no shear stress can be generated. With increasing streamwise coordinate ξ, there is generally a monotonic increase in shear stress which is associated with boundary layer growth along the cylinder periphery, as eloquently noted by Glauert and Lighthill (1955) based on an exceptionally rigorous asymptotic analysis. Figure 22 displays the influence of Soret and Dufour numbers on the Sherwood number. An increase in Dufour number with a concomitant decrease in Soret number is observed to markedly increase the rate of mass transfer. A consistently monotonic decay in Sherwood number is computed i.e. the maximum nanoparticle mass transfer to the cylinder surface arises at the stagnation point and progressively diminishes with increasing streamwise coordinate ξ. This behavior is clearly computable with two-dimensional axisymmetric models (ξ, η) which are easily simulated with the Keller box scheme. Equations (10)–(12) at the stagnation point, $\xi \sim 0$, clearly contract to ordinary differential equations, implying that single-spatial variable models (η) lack the physical rigor for realistic simulations of axisymmetric heat transfer from curved bodies.

It is to be noted that the numerical domain is meshed with 25×25 grid points for visualizing 3D and contour plots. Figure 23 reveals that skin friction factor is strongly augmented with increasing streamwise coordinate ξ until a critical point at which it peaks ($\xi \sim 2$); thereafter, it descends steadily with further streamwise distance, as characterized by the parabolic-type topology. Figures 24 and 25 show that Nusselt number is greatly suppressed with higher M_a and N_T values, i.e. heat transfer rate to the wall is a decreasing function of magnetic field and thermophoresis. This corroborates the earlier computations which have shown that temperature is elevated with stronger magnetic field and thermophoretic body force. Because the pseudoplastic nanofluid is heated with both effects, there is an associated decrement in rate of heat transfer to the cylinder surface (boundary) i.e. lower Nusselt numbers. It is noticed from these figures that the lower Lorentz force and lower thermophoresis have a high rate of heat transfer at the stream coordinate ($\xi \sim 1$). Furthermore, increasing values of the Lorentz force and thermophoresis promotes pseudoplastic nanofluid temperature which leads to reduce heat transfer rate.

Figures 26–28 illustrate the streamlines, isothermal and iso-concentration distributions for various values of streamwise coordinate ξ, magnetic field M_a and buoyancy ratio parameter N_r. Figure 26 shows that the streamlines are denser near the wall (cylinder boundary). It is to be noted that increasing the streamwise coordinate ξ, from 0.5 to 1.5 serves to intensify the streamlines density whereas a subsequent increment in this coordinate from 1.5 to 2.5 manifests in a relaxation in streamlines. Moreover, higher values of magnetic field and buoyancy ratio parameter (progressively stronger species buoyancy, although for $N_r < 1$ thermal buoyancy is dominant) tend to reduce the density of streamlines, which expand in a fan-like manner in the transverse direction (η). Figures 27 and 28 indicate that an increase in the streamwise coordinate ξ, magnetic field and buoyancy ratio parameter, inflate the thermal and mass boundary layer thickness.

Strengthening the magnetic field amplifies the Lorentz force which triggers the electrical conductivity particles in the pseudoplastic nanofluid and tends to increase the fluid temperature and concentration in the pseudoplastic nanofluid, thus increases the heat and mass boundary layer thickness. Generally, N_r is expressed as the ratio of nanoparticle concentration to the thermal buoyancy force. N_r occurs in terms of $\frac{\sin \xi}{\xi}(\theta - N_r \phi)$ in the momentum boundary layer equation. Therefore, nanofluid temperature and nanoparticle concentration are strongly coupled in the nanofluid momentum equation. Hence, thermal and mass boundary layer thickness rise slightly for rising values of N_r. Also, higher values of magnetic field and buoyancy ratio parameter generate an enhancement in heat and mass transfer to the wall, as testified by the lateral fanning in isotherms and iso-concentrations.

5. Conclusion

Motivated by simulating high-temperature magnetic nano-polymer coating flow transport phenomena, a detailed mathematical study has been presented to investigate the thermosolutal (combined natural convection heat and mass transfer) characteristics in radiative pseudoplastic nanofluid boundary layer flow external to a circular cylinder under radial static magnetic field, with variable viscosity, variable thermal conductivity, Soret and Dufour effects. The nanoscale transport is modeled by using the Buongiorno two-component model and the rheological behavior is accommodated by using the Williamson model. Non-similar variables are used to transform the dimensional mass, momentum, energy and nanoparticle concentration (volume fraction) equations into dimensionless form. This nonlinear coupled boundary value problem is solved with the implicit finite difference Keller box method under appropriate wall and free stream boundary conditions. Extensive validation of the solutions with earlier published results is included. The transport properties of the fluid are studied for variation in all thermophysical parameters and visualized as graphs versus transverse coordinate, three-dimensional surface plots, contour plots, streamlines, isothermal and iso-concentration plots. The main findings of the current study are summarized as follows.

- Nanofluid temperature and nanoparticle concentration magnitudes are elevated significantly with increasing magnetic field strength.
- Flow deceleration is induced with larger values of the variable viscosity parameter.
- Higher values of the thermal conductivity parameter enhance velocity and temperature magnitudes.
- An enhancement in Dufour number with a simultaneous decrement in Soret number generates marked flow acceleration and heating, i.e. greater temperature magnitudes.
- An increase in Weissenberg number (i.e. stronger elastic forces relative to viscous forces and greater relaxation time of the pseudoplastic fluid) and thermophoresis parameter increases the nanofluid temperature.
- The density of streamlines is reduced with increasing the magnetic field and buoyancy ratio parameter.
- Higher values of magnetic field and buoyancy ratio parameter boost the isotherms and isoconcentration.

The present study has ignored nanoparticle types, e.g. metallic oxides. This can be considered using the Tiwari–Das formulation in future investigations. Furthermore, ferromagnetic effects may be considered by including magnetic dipoles which also feature in magnetic nano-materials processing systems.

References

Acharya, N., Das, K. and Kundu, P.K. (2019), " "Influence of multiple slips and chemical reaction on radiative MHD Williamson nanofluid flow in porous medium: a computational framework", *Multidiscipline Modeling in Materials and Structures*, Vol. 15 No. 3, pp. 630-658.

Animasaun, I.L. (2015), " Effects of thermophoresis, variable viscosity and thermal conductivity on free convective heat and mass transfer of non-Darcian MHD dissipative Casson fluid flow with suction and nth order of chemical reaction", *Journal of the Nigerian Mathematical Society*, Vol. 34 No. 1, pp. 11-31.

Anoop, K.B., Kabelac, S., Sundararajan, T. and Das, S.K. (2009), "Rheological and flow characteristics of nanofluids: influence of electroviscous effects and particle agglomeration", *Journal of Applied Physics*, Vol. 106 No. 3, p. 34909.

Astanina, M.S., Rashidi, M.M., Sheremet, M.A. and Lorenzini, G. (2019), " Effect of porous insertion on convective energy transport in a chamber filled with a temperature-dependent viscosity liquid in the presence of a heat source term", *International Journal of Heat and Mass Transfer*, Vol. 144, p. 118530.

Basha, H.T., Sivaraj, R., Prasad, V.R. and Beg, O.A. (2020b), "Entropy generation of tangent hyperbolic nanofluid over a circular cylinder in the presence of nonlinear Boussinesq approximation: a non-similar solution", *Journal of Thermal Analysis and Calorimetry*, doi: 10.1007/s10973-020-09981-5.

Basha, H.T., Sivaraj, R., Reddy, A.S. and Chamkha, A.J. (2019), " SWCNH/diamond-ethylene glycol nanofluid flow over a wedge, plate and stagnation point with induced magnetic field and nonlinear radiation-solar energy application", *The European Physical Journal Special Topics*, Vol. 228 No. 12, pp. 2531-2551.

Basha, H.T., Sivaraj, R., Reddy, A.S., Chamkha, A.J. and Tilioua, M. (2020a), " "Impacts of temperature-dependent viscosity and variable Prandtl number on forced convective Falkner-Skan flow of Williamson nanofluid", *SN Applied Sciences*, Vol. 2 No. 3, pp. 477.

Beg, O.A., Bakier, A.Y. and Prasad, V.R. (2009b),"Numerical study of free convection magnetohydrodynamic heat and mass transfer from a stretching surface to a saturated porous medium with Soret and Dufour effects", *Computational Materials Science*, Vol. 46 No. 1, pp. 57-65.

Beg, O.A., Beg, T.A., Bakier, A.Y. and Prasad, V.R. (2009a), " "Chemically reacting mixed convective heat and mass transfer along inclined and vertical plates with Soret and Dufour effects: numerical solutions", *International Journal of Applied Mathematics and Mechanics*, Vol. 5, pp. 39-57.

Beg, O.A., Espinoza, D.E.S., Kadir, A., Shamshuddin, M. and Sohail, A. (2018), "Experimental study of improved rheology and lubricity of drilling fluids enhanced with nanoparticles", *Applied Nanoscience*, Vol. 8 No. 5, pp. 1069-1090.

Beg, O.A., Ferdows, M., Beg, T.A., Ahmed, T., Wahiduzzaman, M. and Alam, M.M. (2016), "Radiative optically dense magnetized transient reactive transport phenomena with cross diffusion and dissipation effects: numerical simulations", *Journal of the Taiwan Institute of Chemical Engineers*, Vol. 66, pp. 12-26.

Beg, O.A., Beg, T.A., Karim, I., Khan, M.S., Alam, M.M., Ferdows, M. and Shamshuddin, M. (2019a), "Numerical study of magneto-convective heat and mass transfer from inclined surface with Soret diffusion and heat generation effects: a model for ocean magnetohydrodynamic energy generator fluid dynamics", *Chinese Journal of Physics*, Vol. 60, pp. 167-179.

Beg, O.A., Kuharat, S., Ferdows, M., Das, M., Kadir, A. and Shamshuddin, M. (2019b), "Modeling magnetic nanopolymer flow with induction and nano-particle solid volume fraction effects: solar magnetic nano-polymer fabrication simulation", *Proceedings of the Institution of Mechanical Engineers, Part N: Journal of Nanomaterials, Nanoengineering and Nanosystems*, Vol. 233 No. 1, pp. 27-45.

Beg, O.A., Prasad, V.R., Vasu, B., Reddy, N.B., Li, Q. and Bhargava, R. (2011), " "Free convection heat and mass transfer from an isothermal sphere to a micropolar regime with Soret/Dufour effects", *International Journal of Heat and Mass Transfer*, Vol. 54 Nos 1/3, pp. 9-18.

Bhatti, M.M., Khalique, C.M., Beg, T., Beg, O.A. and Kadir, A. (2020), "Numerical study of slip and radiative effects on magnetic Fe3O4-water-based nanofluid flow from a nonlinear stretching sheet in porous media with Soret and Dufour diffusion", *Modern Physics Letters B*, Vol. 34 No. 2, p. 2050026.

Bisht, A. and Sharma, R. (2019), "Non-similar solution of Casson nanofluid with variable viscosity and variable thermal conductivity", *International Journal of Numerical Methods for Heat and Fluid Flow*, Vol. 22, pp. 3919-3938.

Buongiorno, J. (2006), "Convective transport in nanofluids", *Journal of Heat Transfer*, Vol. 128 No. 3, p. 240.

Cebeci, T. and Bradshaw, P. (1984), *Physical and Computational Aspects of Convective Heat Transfer*, Springer, New York, NY.

Chang, H., Lee, W.S. and Lee, J. (2019), "Rheological characteristics of non-Newtonian GPTMS-SiO2 nanofluids", *International Communications in Heat and Mass Transfer*, Vol. 106, pp. 38-45.

Das, S.K., Choi, S.U.S., Yu, W. and Pradeep, T. (2007), *Nanofluids: Science and Technology*, *Wiley-Interscience*, New York, NY.

Dhumal, J., Bandgar, S., Zipare, K. and Shahane, G. (2015), "Fe_3O_4 ferrofluid nanoparticles: synthesis and rheological behavior", *International Journal of Materials Chemistry and Physics*, Vol. 1, pp. 141-145.

Durairaj, M., Ramachandran, S. and Mehdi, R.M. (2017), " Heat generating/absorbing and chemically reacting Casson fluid flow over a vertical cone and flat plate saturated with non-Darcy porous medium", *International Journal of Numerical Methods for Heat and Fluid Flow*, Vol. 27 No. 1, pp. 156-173.

Gaffar, S.A., Prasad, V.R. and Beg, O.A. (2015), " "Numerical study of flow and heat transfer of non-Newtonian tangent hyperbolic fluid from a sphere with Biot number effects", *Alexandria Engineering Journal*, Vol. 54 No. 4, pp. 829-841.

Glauert, M.B. and Lighthill, M.J. (1955), "The axisymmetric boundary layer on a long thin cylinder", *Proceedings of The Royal Society of London, Series A*, Vol. 224, p. 188.

Hayat, T., Khan, M.I., Farooq, M., Gull, N. and Alsaedi, A. (2016), " "Unsteady three-dimensional mixed convection flow with variable viscosity and thermal conductivity", *Journal of Molecular Liquids*, Vol. 223, pp. 1297-1310.

Hong, R.Y., Ren, Z.Q., Han, Y.P., Li, H.Z., Zheng, Y. and Ding, J. (2007), " Rheological properties of water based Fe_3O_4 ferrofluids", *Chemical Engineering Science*, Vol. 62 No. 21, pp. 5912-5924.

Hussanan, A., Salleh, M.Z., Khan, I. and Shafie, S. (2017), "Convection heat transfer in micropolar nanofluids with oxide nanoparticles in water, kerosene and engine oil", *Journal of Molecular Liquids*, Vol. 229, pp. 482-488.

Jaluria, Y. (2013), "Thermal issues in materials processing", *Journal of Heat Transfer*, Vol. 135 No. 6, p. 61701.

Kafoussias, N.G. and Williams, E.W. (1995), " "The effect of temperature-dependent viscosity on free-forced convective laminar boundary layer flow past a vertical isothermal flat plate", *Acta Mechanica*, Vol. 110 Nos 1/4, pp. 123-137.

Kang, J., Zhou, F., Tan, W. and Xia, T. (2014), "Thermal instability of a nonhomogeneous power-law nanofluid in a porous layer with horizontal through flow", *Journal of Non-Newtonian Fluid Mechanics*, Vol. 213, pp. 50-56.

Keller, H.B. (1971), "A new difference scheme for parabolic problems", *in numerical solution of partial differential equations - II, synspade 1970, Academic press: Inc.* pp. 327-350.

Khan, M.I., Nigar, M., Hayat, T. and Alsaedi, A. (2019), " On the numerical simulation of stagnation point flow of non-Newtonian fluid (Carreau fluid) with Cattaneo–Christov heat flux", *Computer Methods and Programs in Biomedicine*, Vol. 187, p. 105221.

Kumar, B.R. and Sivaraj, R. (2013), "Heat and mass transfer in MHD viscoelastic fluid flow over a vertical cone and flat plate with variable viscosity", *International Journal of Heat and Mass Transfer*, Vol. 56 Nos 1/2, pp. 370-379.

Kumar, B.R. and Sivaraj, R. (2013), "MHD viscoelastic fluid non-Darcy flow over a vertical cone and a flat plate", *International Communications in Heat and Mass Transfer*, Vol. 40, pp. 1-6.

Latiff, N.A., Uddin, M.J., Beg, O.A. and Ismail, A.I.M. (2016), " Unsteady forced bioconvection slip flow of a micropolar nanofluid from a stretching/shrinking sheet", *Proceedings of the Institution of Mechanical Engineers, Part N: Journal of Nanomaterials, Nanoengineering and Nanosystems*, Vol. 230 No. 4, pp. 177-187.

Ma, Y., Mohebbi, R., Rashidi, M.M., Manca, O. and Yang, Z. (2019), "Numerical investigation of MHD effects on nanofluid heat transfer", *Journal of Thermal Analysis and Calorimetry*, Vol. 135 No. 6, pp. 3197-3213.

Makinde, O.D. and Chinyoka, T. (2012), "Analysis of unsteady flow of a variable viscosity reactive fluid in a slit with wall suction or injection", *Journal of Petroleum Science and Engineering*, Vol. 94-95, pp. 1-11.

Makinde, O.D. and Olanrewaju, P.O. (2011a), " "Unsteady mixed convection with Soret and Dufour effects past a porous plate moving through a binary mixture of chemically reacting fluid", *Chemical Engineering Communications*, Vol. 198 No. 7, pp. 920-938.

Makinde, O.D., Chinyoka, T. and Rundora, L. (2011b), "Unsteady flow of a reactive variable viscosity non-Newtonian fluid through a porous saturated medium with asymmetric convective boundary conditions", *Computers and Mathematics with Applications*, Vol. 62 No. 9, pp. 3343-3352.

Malik, M.Y., Bibi, M., Khan, F. and Salahuddin, T. (2016), "Numerical solution of Williamson fluid flow past a stretching cylinder and heat transfer with variable thermal conductivity and heat generation/absorption", *AIP Advances*, Vol. 6 No. 3, p. 35101.

Manjunatha, S. and Gireesha, B.J. (2016), " "Effects of variable viscosity and thermal conductivity on MHD flow and heat transfer of a dusty fluid", *Ain Shams Engineering Journal*, Vol. 7 No. 1, pp. 505-515.

Mansoury, D., Doshmanziari, F.I., Rezaie, S. and Rashidi, M.M. (2019), "Effect of Al_2O_3/water nanofluid on performance of parallel flow heat exchangers", *Journal of Thermal Analysis and Calorimetry*, Vol. 135 No. 1, pp. 625-643.

Mehmood, R., Tabassum, R., Kuharat, S., Beg, O.A. and Babie, M. (2019), "Thermal slip in oblique radiative nano-polymer gel transport with temperature-dependent viscosity: solar collector nanomaterial coating manufacturing simulation", *Arabian Journal for Science and Engineering*, Vol. 44 No. 2, pp. 1525-1541.

Merkin, J.H. (1977), "Free convection boundary layers on cylinders of elliptic cross section", *Journal of Heat Transfer*, Vol. 99 No. 3, pp. 453-457.

Modest, M. (1992), *Radiative Heat Transfer*, MacGraw-Hill, New York, NY.

Muthtamilselvan, M., Periyadurai, K. and Hee, D. (2018), "Impact of nonuniform heated plate on double-diffusive natural convection of micropolar fluid in a square cavity with Soret and Dufour effects", *Advanced Powder Technology*, Vol. 29 No. 1, pp. 66-77.

Nadeem, S., Ahmad, S. and Muhammad, N. (2017), "Cattaneo-Christov flux in the flow of a viscoelastic fluid in the presence of Newtonian heating", *Journal of Molecular Liquids*, Vol. 237, pp. 180-184.

Nasrin, R. and Alim, M.A. (2009), "MHD free convection flow along a vertical flat plate with thermal conductivity and viscosity depending on temperature", *Journal of Naval Architecture and Marine Engineering*, Vol. 6 No. 2, pp. 72-83.

Norouzi, M., Daghighi, S.Z. and Beg, O.A. (2018), "Exact analysis of heat convection of viscoelastic FENE-P fluids through isothermal slits and tubes", *Meccanica*, Vol. 53 Nos 4/5, pp. 817-831.

Pal, D., Mandal, G. and Vajravalu, K. (2016), "Soret and Dufour effects on MHD convective – radiative heat and mass transfer of nanofluids over a vertical non-linear stretching/shrinking sheet", *Applied Mathematics and Computation*, Vols 287/288, pp. 184-200.

Prasad, V.R., Gaffar, S.A. and Kumar, B.R. (2019), "Non-similar computational solutions for double-diffusive MHD transport phenomena for non-Newtonian nanofluid from a horizontal circular cylinder", *Nonlinear Engineering*, Vol. 485, p. 8470.

Raju, C.S.K. and Sandeep, N. (2016), "Heat and mass transfer in MHD non-Newtonian bio-convection flow over a rotating cone/plate with cross diffusion", *Journal of Molecular Liquids*, Vol. 215, pp. 115-126.

Rashad, A. and Chamkha, A.J. (2014), " Heat and mass transfer by natural convection flow about a truncated cone in porous media with Soret and Dufour effects", *International Journal of Numerical Methods for Heat and Fluid Flow*, Vol. 24, pp. 595-612.

Reddy, P.S. and Chamkha, A.J. (2016), "Soret and Dufour effects on MHD convective flow of Al_2O_3 - water and TiO_2 - water nanofluids past a stretching sheet in porous media with heat generation/absorption", *Advanced Powder Technology*, Vol. 27 No. 4, pp. 1207-1218.

Reddy, G.J., Kumar, M. and Beg, O.A. (2018), "Effect of temperature dependent viscosity on entropy generation in transient viscoelastic polymeric fluid flow from an isothermal vertical plate", *Physica A: Statistical Mechanics and Its Applications*, Vol. 510, pp. 426-445.

Ruhaila, M.K., Sivasankaran, S., Bhuvaneswari, M. and Hussein, A.K. (2017), "Analytical and numerical study on convection of nanofluid past a moving wedge with Soret and Dufour effects", *International Journal of Numerical Methods for Heat and Fluid Flow*, Vol. 27, pp. 2333-2354.

Salahuddin, T., Muhammad, S. and Sakinder, S. (2019), " Impact of generalized heat and mass flux models on Darcy–Forchheimer Williamson nanofluid flow with variable viscosity", *Physica Scripta*, Vol. 94 No. 12, p. 125201.

Sansom, C.L., Jones, P., Dorey, R.A., Beck, C., Stanhope-Bosumpim, A. and Peterson, J. (2013),"Synthesis and characterization of Mn0.5Zn0.5Fe2O4 and Fe3O4 nanoparticle ferrofluids for thermo-electric conversion", *Journal of Magnetism and Magnetic Materials*, Vol. 335, pp. 159-162.

Sheikholeslami, M. and Rokni, H.B. (2017), "Magnetic nanofluid natural convection in the presence of thermal radiation considering variable viscosity", *The European Physical Journal – Plus*, Vol. 132, p. 238.

Sheparovych, R., Sahoo, Y., Motornov, M., Wang, S., Luo, H., Prasad, P.N., Sokolov, I. and Minko, S. (2006), "Polyelectrolyte stabilized nanowires from Fe3O4 nanoparticles via magnetic field induced self -assembly", *Chemistry of Materials*, Vol. 18 No. 3, pp. 591-593.

Sivaraj, R., Benazir, A.J., Srinivas, S. and Chamkha, A.J. (2019), " "Investigation of cross-diffusion effects on casson fluid flow in existence of variable fluid properties", *The European Physical Journal Special Topics*, Vol. 228 No. 1, pp. 35-53.

Subbarayudu, K., Suneetha, S. and Reddy, P.B.A. (2020), " "The assessment of time dependent flow of williamson fluid with radiative blood flow against a wedge", *Propulsion and Power Research*, Vol. 9 No. 1, pp. 87-99.

Vshivkov, S.A. and Rusinova, E. (2017), " "Effect of magnetic field on the rheological properties of poly (ethylene glycol) and poly (dimethylsiloxane) mixtures with aerosil and iron nanoparticles", *Polymer Science, Series A*, Vol. 59 No. 5, pp. 764-771.

Williamson, R.V. (1929), "The flow of pseudoplastic materials", *Industrial and Engineering Chemistry Research*, Vol. 11, pp. 1108-1111.

Yih, K.A. (2000), " "Effect of uniform blowing/suction on MHD-natural convection over a horizontal cylinder: UWT or UHF", *Acta Mechanica*, Vol. 144 Nos 1/2, pp. 17-27.

Appendix

To linearize the nonlinear system of equations using Newton's method, we introduce the following iterates:

$$\omega f_j^{(n)} = f_j^{(n+1)} - f_j^{(n)},$$

$$\omega u_j^{(n)} = u_j^{(n+1)} - u_j^{(n)},$$

$$\omega v_j^{(n)} = v_j^{(n+1)} - v_j^{(n)},$$

$$\omega s_j^{(n)} = s_j^{(n+1)} - s_j^{(n)},$$

$$\omega t_j^{(n)} = t_j^{(n+1)} - t_j^{(n)},$$

$$\omega g_j^{(n)} = g_j^{(n+1)} - g_j^{(n)},$$

$$\omega p_j^{(n)} = p_j^{(n+1)} - p_j^{(n)}$$

Implementing the above expressions in equations (30)–(36) and neglecting higher-order terms of ω, leads to:

$$\omega f_j - \omega f_{j-1} - \frac{h_j}{2}\omega u_j - \frac{h_j}{2}\omega u_{j-1} - (e_1)_j = 0 \tag{A.1}$$

$$\omega u_j - \omega u_{j-1} - \frac{h_j}{2}\omega v_j - \frac{h_j}{2}\omega v_{j-1} - (e_2)_j = 0 \tag{A.2}$$

$$\omega s_j - \omega s_{j-1} - \frac{h_j}{2}\omega t_j - \frac{h_j}{2}\omega t_{j-1} - (e_3)_j = 0 \tag{A.3}$$

$$\omega g_j - \omega g_{j-1} - \frac{h_j}{2}\omega p_j - \frac{h_j}{2}\omega p_{j-1} - (e_4)_j = 0 \tag{A.4}$$

$$\begin{aligned}(a_1)_j\omega v_j + (a_2)_j\omega v_{j-1} + (a_3)_j\omega f_j + (a_4)_j\omega f_{j-1} + (a_5)_j\omega u_j + (a_6)_j\omega u_{j-1} + (a_7)_j\omega s_j \\ +(a_8)_j\omega s_{j-1} + (a_9)_j\omega t_j + (a_{10})_j\omega t_{j-1} + (a_{11})_j\omega g_j + (a_{12})_j\omega g_{j-1} - (e_5)_{j-1/2} = 0,\end{aligned} \tag{A.5}$$

$$(b_1)_j\omega t_j + (b_2)_j\omega t_{j-1} + (b_3)_j\omega f_j + (b_4)_j\omega f_{j-1} + (b_5)_j\omega u_j + (b_6)_j\omega u_{j-1} + (b_7)_j\omega s_j + (b_8)_j\omega s_{j-1} + (b_9)_j\omega p_j + (b_{10})_j\omega p_{j-1} - (e_6)_{j-1/2} = 0 \tag{A.6}$$

$$(c_1)_j\omega p_j + (c_2)_j\omega p_{j-1} + (c_3)_j\omega f_j + (c_4)_j\omega f_{j-1} + (c_5)_j\omega u_j + (c_6)_j\omega u_{j-1} + (c_7)_j\omega g_j + (c_8)_j\omega g_{j-1} + (c_9)_j\omega t_j + (c_{10})_j\omega t_{j-1} - (e_7)_{j-1/2} = 0, \tag{A.7}$$

where

$$(a_1)_j = 1 - \gamma^* s_{j-1/2} + 2We\xi v_{j-1/2} - 2We\xi\gamma^* v_{j-1/2}s_{j-1/2} + h_j\left[-We\xi\gamma^* v_{j-1/2}t_{j-1/2} - \frac{\gamma^*}{2}f_{j-1/2} + \frac{(1+\alpha)}{2}f_{j-1/2} - \frac{\alpha}{2}f_{j-1/2}^{n-1}\right],$$

$$(a_2)_j = -\left(1 - \gamma^* s_{j-1/2} + 2We\xi v_{j-1/2} - 2We\xi\gamma^* v_{j-1/2}s_{j-1/2}\right) + h_j\left[-We\xi\gamma^* v_{j-1/2}t_{j-1/2} - \frac{\gamma^*}{2}f_{j-1/2} + \frac{(1+\alpha)}{2}f_{j-1/2} - \frac{\alpha}{2}f_{j-1/2}^{n-1}\right]$$

$$(a_3)_j = h_j\left[\frac{(1+\alpha)}{2}v_{j-1/2} + \frac{\alpha}{2}v_{j-1/2}^{n-1}\right],$$

$$(a_4)_j = (a_3)_j,$$

$$(a_5)_j = h_j\left[-(1+\alpha)u_{j-1/2} - \frac{1}{2}(M_a)\right],$$

$$(a_6)_j = (a_5)_j,$$

$$(a_7)_j = -\frac{\gamma^*}{2}(v_j - v_{j-1}) - We\xi\gamma^*(v_j - v_{j-1})v_{j-1/2} + \frac{B}{2}h_j,$$

$$(a_8)_j = (a_7)_j,$$

$$(a_9)_j = h_j\left[-\frac{We\xi\gamma^*}{2}(v_{j-1/2})^2 - \frac{\gamma^*}{2}(v_{j-1/2})\right],$$

$$(a_{10})_j = (a_9)_j,$$

$$(a_{11})_j = -\frac{B}{2} h_j N_r,$$

$$(a_{12})_j = (a_{11})_j,$$

$$(b_1)_j = \frac{1}{\mathrm{Pr}}\left[1 + \frac{4}{3R_a} + \delta^* s_{j-1/2}\right] + h_j\left[\frac{\delta^*}{\mathrm{Pr}} t_{j-1/2} + \frac{N_B}{2} p_{j-1/2} + N_T t_{j-1/2} + \frac{(1+\alpha)}{2} f_{j-1/2} - \frac{\alpha}{2} f^{n-1}_{j-1/2}\right],$$

$$(b_2)_j = -\frac{1}{\mathrm{Pr}}\left[1 + \frac{4}{3R_a} + \delta^* s_{j-1/2}\right] + h_j\left[\frac{\delta^*}{\mathrm{Pr}} t_{j-1/2} + \frac{N_B}{2} p_{j-1/2} + N_T p_{j-1/2} + \frac{(1+\alpha)}{2} f_{j-1/2} - \frac{\alpha}{2} f^{n-1}_{j-1/2}\right],$$

$$(b_3)_j = h_j\left[\frac{(1+\alpha)}{2} t_{j-1/2} + \frac{\alpha}{2} t^{n-1}_{j-1/2}\right],$$

$$(b_4)_j = (b_3)_j,$$

$$(b_5)_j = h_j\left[-\frac{\alpha}{2} s_{j-1/2} + \frac{\alpha}{2} s^{n-1}_{j-1/2}\right],$$

$$(b_6)_j = (b_5)_j,$$

$$(b_7)_j = \frac{\delta^*}{2\mathrm{Pr}}(t_j - t_{j-1}) + h_j\left[-\frac{\alpha}{2} u_{j-1/2} - \frac{\alpha}{2} u^{n-1}_{j-1/2}\right],$$

$$(b_8)_j = (b_7)_j,$$

$$(b_9)_j = h_j\left[\frac{N_B}{2} t_{j-1/2}\right] + D_u,$$

$$(b_{10})_j = h_j\left[\frac{N_B}{2} t_{j-1/2}\right] - D_u$$

$$(c_1)_j = \frac{1}{Sc} + h_j\left[\frac{(1+\alpha)}{2} f_{j-1/2} - \frac{\alpha}{2} f_{j-1/2}^{n-1}\right],$$

$$(c_2)_j = -\frac{1}{Sc} + h_j\left[\frac{(1+\alpha)}{2} f_{j-1/2} - \frac{\alpha}{2} f_{j-1/2}^{n-1}\right],$$

$$(c_3)_j = h_j\left[\frac{(1+\alpha)}{2} p_{j-1/2} + \frac{\alpha}{2} p_{j-1/2}^{n-1}\right],$$

$$(c_4)_j = (c_3)_j,$$

$$(c_5)_j = h_j\left[-\frac{\alpha}{2} g_{j-1/2} + \frac{\alpha}{2} g_{j-1/2}^{n-1}\right],$$

$$(c_6)_j = (c_5)_j,$$

$$(c_7)_j = h_j\left[-\frac{\alpha}{2} u_{j-1/2} - \frac{\alpha}{2} u_{j-1/2}^{n-1}\right],$$

$$(c_8)_j = (c_7)_j,$$

$$(c_9)_j = \frac{1}{Sc}\frac{N_T}{N_B} + S_r,$$

$$(c_{10})_j = -(c_9)_j,$$

$$\begin{aligned}(e_5)_{j-1/2} = {} & (v_{j-1} - v_j)\left[1 - \gamma^* s_{j-1/2} + 2We\xi v_{j-1/2} - 2We\xi\gamma^* v_{j-1/2} s_{j-1/2}\right] \\ & + We\xi\gamma^* h_j t_{j-1/2}(v_{j-1/2})^2 - (1+\alpha) h_j f_{j-1/2} v_{j-1/2} + h_j(1+\alpha) u_{j-1/2}^2 \\ & + (M_a) h_j u_{j-1/2} + \gamma^* h_j v_{j-1/2} t_{j-1/2} - \alpha h_j v_{j-1/2}^{n-1} f_{j-1/2} + \alpha h_j f_{j-1/2}^{n-1} v_{j-1/2} \\ & - B h_j\left[s_{j-1/2} - N_r(g_{j-1/2})\right] + (E_1)_{j-1/2}^{i-1},\end{aligned} \tag{A.8}$$

$$\begin{aligned}(e_6)_{j-1/2} = {} & \frac{1}{\mathrm{Pr}}(t_{j-1} - t_j)\left[1 + \frac{4}{3R_a} + \delta^* s_{j-1/2}\right] - \frac{\delta^*}{\mathrm{Pr}} h_j (t_{j-1/2})^2 - N_B h_j t_{j-1/2} p_{j-1/2} \\ & - N_T h_j (t_{j-1/2})^2 - (1+\alpha) h_j f_{j-1/2} t_{j-1/2} + h_j \alpha u_{j-1/2} s_{j-1/2} - \alpha h_j s_{j-1/2}^{n-1} u_{j-1/2} \\ & + \alpha h_j u_{j-1/2}^{n-1} s_{j-1/2} + \alpha h_j f_{j-1/2}^{n-1} t_{j-1/2}, - \alpha h_j t_{j-1/2}^{n-1} f_{j-1/2} + D_u(p_{j-1} - p_j) \\ & + (E_2)_{j-1/2}^{i-1},\end{aligned} \tag{A.9}$$

$$(e_7)_{j-1/2} = \frac{1}{Sc}(p_{j-1} - p_j) - (1+\alpha)h_j f_{j-1/2} p_{j-1/2} + h_j \alpha u_{j-1/2} g_{j-1/2} - \alpha h_j g^{n-1}_{j-1/2} u_{j-1/2} + \alpha h_j u^{n-1}_{j-1/2} g_{j-1/2} + \alpha h_j f^{n-1}_{j-1/2} p_{j-1/2} - \alpha h_j p^{n-1}_{j-1/2} f_{j-1/2} + \left[\frac{1}{Sc}\frac{N_T}{N_B} + S_r\right](t_{j-1} - t_j) + (E_3)^{i-1}_{j-1/2}. \quad \text{(A.10)}$$

The boundary conditions (29) emerge as following:

$$\begin{aligned} &\omega f_0 = 0, \ \omega u_0 = 0, \ \omega s^n_0 = 0, \ \omega g_0 = 0, \\ &\omega u_J = 0, \ \omega s_J = 0, \ \omega g_J = 0, \ f^n_0 = u^n_0 = 0, \\ &s^n_0 = 1, \ g^n_0 = 1, \ u^n_J = 0, \ s^n_J = 0, \ g^n_J = 0 \end{aligned}$$

Step 4: The block-elimination method is used to compute the linearized difference equations (A.1)–(A.10) as outlined by Cebeci and Bradshaw (1984) using the matrix-vector form:

$$A\omega = e$$

where

$$A = \begin{bmatrix} [A_1] & [C_1] & & & & & \\ [B_2] & [A_2] & [C_2] & & & & \\ & & \ddots & & & & \\ & & & \ddots & & & \\ & & & & \ddots & & \\ & & & & [B_{J-1}] & [A_{J-1}] & [C_{J-1}] \\ & & & & & [B_J] & [C_J] \end{bmatrix}, \quad \omega = \begin{bmatrix} [\omega_1] \\ [\omega_2] \\ \vdots \\ [\omega_{J-1}] \\ [\omega_J] \end{bmatrix}, \quad e = \begin{bmatrix} [e_1] \\ [e_2] \\ \vdots \\ [e_{J-1}] \\ [e_J] \end{bmatrix}.$$

The elements of the matrices are as follows:

$$[A_1] = \begin{bmatrix} 0 & 0 & 0 & 1 & 0 & 0 & 0 \\ -\frac{h_j}{2} & 0 & 0 & 0 & -\frac{h_j}{2} & 0 & 0 \\ 0 & -\frac{h_j}{2} & 0 & 0 & 0 & -\frac{h_j}{2} & 0 \\ 0 & 0 & -\frac{h_j}{2} & 0 & 0 & 0 & -\frac{h_j}{2} \\ (a_2)_1 & 0 & (a_{10})_1 & (a_3)_1 & (a_1)_1 & 0 & (a_9)_1 \\ 0 & (b_{10})_1 & (b_2)_1 & (b_3)_1 & 0 & (b_9)_1 & (b_1)_1 \\ 0 & (c_2)_1 & (c_{10})_1 & (c_3)_1 & 0 & (c_1)_1 & (c_9)_1 \end{bmatrix},$$

$$[A_J] = \begin{bmatrix} -\frac{h_j}{2} & 0 & 0 & 1 & 0 & 0 & 0 \\ -1 & 0 & 0 & 0 & -\frac{h_j}{2} & 0 & 0 \\ 0 & -1 & 0 & 0 & 0 & -\frac{h_j}{2} & 0 \\ 0 & 0 & -1 & 0 & 0 & 0 & -\frac{h_j}{2} \\ (a_6)_j & (a_{12})_j & (a_8)_j & (a_3)_j & (a_1)_j & 0 & (a_9)_j \\ (b_6)_j & 0 & (b_8)_j & (b_3)_j & 0 & (b_9)_j & (b_1)_j \\ (c_6)_j & (c_8)_j & 0 & (c_3)_j & 0 & (c_1)_j & (c_9)_j \end{bmatrix}, \quad 2 \le j \le J$$

$$[B_J] = \begin{bmatrix} 0 & 0 & 0 & -1 & 0 & 0 & 0 \\ 0 & 0 & 0 & 0 & -\frac{h_j}{2} & 0 & 0 \\ 0 & 0 & 0 & 0 & 0 & -\frac{h_j}{2} & 0 \\ 0 & 0 & 0 & 0 & 0 & 0 & -\frac{h_j}{2} \\ 0 & 0 & 0 & (a_4)_j & (a_2)_j & 0 & (a_{10})_j \\ 0 & 0 & 0 & (b_4)_j & 0 & (b_{10})_j & (b_2)_j \\ 0 & 0 & 0 & (c_4)_j & 0 & (c_2)_j & (c_{10})_j \end{bmatrix}, \quad 2 \le j \le J$$

$$[C_J] = \begin{bmatrix} -\frac{h_j}{2} & 0 & 0 & 0 & 0 & 0 & 0 \\ 1 & 0 & 0 & 0 & 0 & 0 & 0 \\ 0 & 1 & 0 & 0 & 0 & 0 & 0 \\ 0 & 0 & 1 & 0 & 0 & 0 & 0 \\ (a_5)_j & (a_{11})_j & (a_7)_j & 0 & 0 & 0 & 0 \\ (b_5)_j & 0 & (b_7)_j & 0 & 0 & 0 & 0 \\ (c_5)_j & (c_7)_j & 0 & 0 & 0 & 0 & 0 \end{bmatrix}, \quad 1 \le j \le J-1$$

$$[\omega_1] = \begin{bmatrix} \omega v_0 \\ \omega p_0 \\ \omega t_0 \\ \omega f_1 \\ \omega v_1 \\ \omega p_1 \\ \omega t_1 \end{bmatrix}, \qquad [\omega_j] = \begin{bmatrix} \omega u_{j-1} \\ \omega g_{j-1} \\ \omega s_{j-1} \\ \omega f_j \\ \omega v_j \\ \omega p_j \\ \delta t_j \end{bmatrix}, \quad 2 \le j \le J$$

$$\text{and } [e_j] = \begin{bmatrix} (e_1)_{j-(1/2)} \\ (e_2)_{j-(1/2)} \\ (e_3)_{j-(1/2)} \\ (e_4)_{j-(1/2)} \\ (e_5)_{j-(1/2)} \\ (e_6)_{j-(1/2)} \\ (e_7)_{j-(1/2)} \end{bmatrix}, \quad 1 \le j \le J$$

Physical parameters	Values	Physical quantities	ξ 0	0.5	1	1.5	2	2.5	CPU time(s)
		C_f^*	0	0.2521	0.4667	0.5634	0.5959	0.4613	
	0.0	Nu^*	0.6688	0.6499	0.6256	0.5798	0.5282	0.4504	8.757743
		Sh^*	0.1758	0.1710	0.1646	0.1527	0.1391	0.1188	
		C_f^*	0	0.2006	0.3612	0.4178	0.4047	0.2421	
M_a	0.5	Nu^*	0.5839	0.5645	0.5338	0.4802	0.4118	0.3056	9.832399
		Sh^*	0.1542	0.1492	0.1411	0.1272	0.1093	0.0814	
		C_f^*	0	0.1681	0.2968	0.3344	0.3061	0.1558	
	1.0	Nu^*	0.5206	0.5009	0.4666	0.4089	0.3318	0.2136	10.132770
		Sh^*	0.1385	0.1334	0.1245	0.1095	0.0893	0.0581	
		C_f^*	0	0.1463	0.2554	0.2837	0.2521	0.1206	
	1.5	Nu^*	0.4744	0.4549	0.4195	0.3614	0.2835	0.1692	9.951370
		Sh^*	0.1274	0.1223	0.1132	0.0981	0.0778	0.0473	
	0.15	C_f^*	0	0.1974	0.3552	0.4109	0.3977	0.2374	
	&	Nu^*	0.5919	0.5722	0.5411	0.4867	0.4172	0.3087	8.980526
	0.4	Sh^*	0.1391	0.1347	0.1276	0.1152	0.0992	0.0742	
	0.3	C_f^*	0	0.1988	0.3577	0.4137	0.4006	0.2393	
D_u&S_r	&	Nu^*	0.5913	0.5716	0.5405	0.4860	0.4166	0.3086	12.504586
	0.2	Sh^*	0.1465	0.1418	0.1342	0.1210	0.1041	0.0776	
	0.6	C_f^*	0	0.2006	0.3612	0.4178	0.4047	0.2421	
	&	Nu^*	0.5839	0.5645	0.5338	0.4802	0.4118	0.3056	14.960204
	0.1	Sh^*	0.1542	0.1492	0.1411	0.1272	0.1093	0.0814	
	0.8	C_f^*	0	0.2019	0.3634	0.4204	0.4073	0.2439	
	&	Nu^*	0.5774	0.5582	0.5279	0.4750	0.4075	0.3029	9.496180
	0.075	Sh^*	0.1584	0.1532	0.1450	0.1306	0.1122	0.0836	

Table A1. Impacts of M_a and D_u and S_r on local skin friction coefficient (C_f^*), dimensionless local rate of heat transfer (Nu^*) and dimensionless local rate of mass transfer (Sh^*) for various values of ξ

Table A2.
Impacts of N_r and R_a on local skin friction coefficient (C_f^*), dimensionless local rate of heat transfer (Nu^*) and dimensionless local rate of mass transfer (Sh^*) for various values of ξ

Physical parameters	Values	Physical quantities	ξ 0	0.5	1	1.5	2	2.5	CPU time (s)
		C_f^*	0	0.3210	0.5917	0.6793	0.6852	0.4260	
	0.1	Nu^*	0.6997	0.6749	0.6419	0.5792	0.5055	0.3873	9.280738
		Sh^*	0.1838	0.1774	0.1688	0.1523	0.1330	0.1020	
		C_f^*	0	0.2631	0.4797	0.5531	0.5481	0.3359	
N_r	0.3	Nu^*	0.6478	0.6256	0.5934	0.5348	0.4631	0.3503	9.395184
		Sh^*	0.1704	0.1647	0.1563	0.1409	0.1222	0.0926	
		C_f^*	0	0.2006	0.3612	0.4178	0.4047	0.2421	
	0.5	Nu^*	0.5839	0.5645	0.5338	0.4802	0.4118	0.3056	8.220380
		Sh^*	0.1542	0.1492	0.1411	0.1272	0.1093	0.0814	
		C_f^*	0	0.0941	0.1652	0.1909	0.1746	0.0967	
	0.8	Nu^*	0.4480	0.4344	0.4093	0.3677	0.3102	0.2203	7.504675
		Sh^*	0.1211	0.1176	0.1112	0.1004	0.0854	0.0614	
		C_f^*	0	0.2287	0.4134	0.4791	0.4674	0.2867	
	0.1	Nu^*	1.4922	1.4514	1.3847	1.2702	1.1242	0.9021	12.398441
		Sh^*	0.2309	0.2229	0.2116	0.1910	0.1657	0.1259	
		C_f^*	0	0.2103	0.3791	0.4388	0.4261	0.2570	
R_a	0.3	Nu^*	0.7667	0.7420	0.7026	0.6341	0.5467	0.4123	12.864155
		Sh^*	0.1828	0.1766	0.1673	0.1507	0.1299	0.0974	
		C_f^*	0	0.2006	0.3612	0.4178	0.4047	0.2421	
	0.5	Nu^*	0.5839	0.5645	0.5338	0.4802	0.4118	0.3056	16.059574
		Sh^*	0.1542	0.1492	0.1411	0.1272	0.1093	0.0814	
		C_f^*	0	0.1922	0.3457	0.3998	0.3867	0.2300	
	0.8	Nu^*	0.4651	0.4496	0.4252	0.3823	0.3276	0.2414	14.713669
		Sh^*	0.1257	0.1220	0.1158	0.1049	0.0907	0.0681	

About the authors

Thameem Basha Hayath is Research Associate in the Department of Mathematics, School of Advanced Sciences, Vellore Institute of Technology, Vellore, India. His area of research is in fluid dynamics. He is pursuing PhD under the supervision of Dr R. Sivaraj from the Vellore Institute of Technology.

Dr Sivaraj Ramachandran is Senior Assistant Professor in the Department of Mathematics, School of Advanced Sciences, Vellore Institute of Technology, Vellore, India. His area of research is in fluid dynamics. He has published 35 research articles in SCOPUS indexed journals. He has received more than 450 citations and his h-index is 13. Sivaraj Ramachandran is the corresponding author and can be contacted at: sivaraj.kpm@gmail.com

Dr Ramachandra Prasad Vallampati is a Professor in the Department of Mathematics, School of Advanced Sciences, Vellore Institute of Technology, Vellore, India. His area of research is in fluid dynamics and CFD. He has published more than 142 research articles and received more than 2000 citations. He has an h-index of 25 in the field of fluid dynamics and CFD.

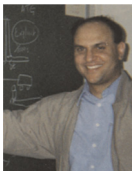

Dr O. Anwar Bég is Professor of Engineering Science and Director of the Multi-Physical Engineering Sciences Group (MPESG), Department of Aeronautical/Mechanical Engineering Department, School of Science, Engineering and Environment (SEE), University of Salford, Manchester, UK. His areas of research are medical, energy, corrosion, electromagnetic fuel cell, bio-propulsion, rocket thermoelasticity and smart materials engineering. He has published more than 500 journal papers, 5 books, many book chapters and conference articles. His h-index is 55 and he has received over 12,000 citations on google scholar. In 2018, he won the University of Salford Vice Chancellor Research Excellence Award for his contributions in computational fluid dynamics, biomechanics and nanoscale engineering.